FeO-Enabled Low-Temperature CO_2-Splitting for Chemical Looping Carbon Utilization

Supplementary Information

Huang-Chin Lin†, Yi Chen†, Tzu-Hao Hung, Ding-Huei Tsai, Lu-Yu Chueh, Chun-I Chou, Kun-Han Lin, Yung-Tin (Frank) Pan**

Department of Chemical Engineering, National Tsing Hua University

101 Sec. 2., Kuang-Fu Rd., Hsinchu, Taiwan, 300044

*Email: ytpan@mx.nthu.edu.tw; kunhan.lin@mx.nthu.edu.tw

KEYWORDS Chemical looping, CO_2 utilization, iron oxide, FeO, RWGS

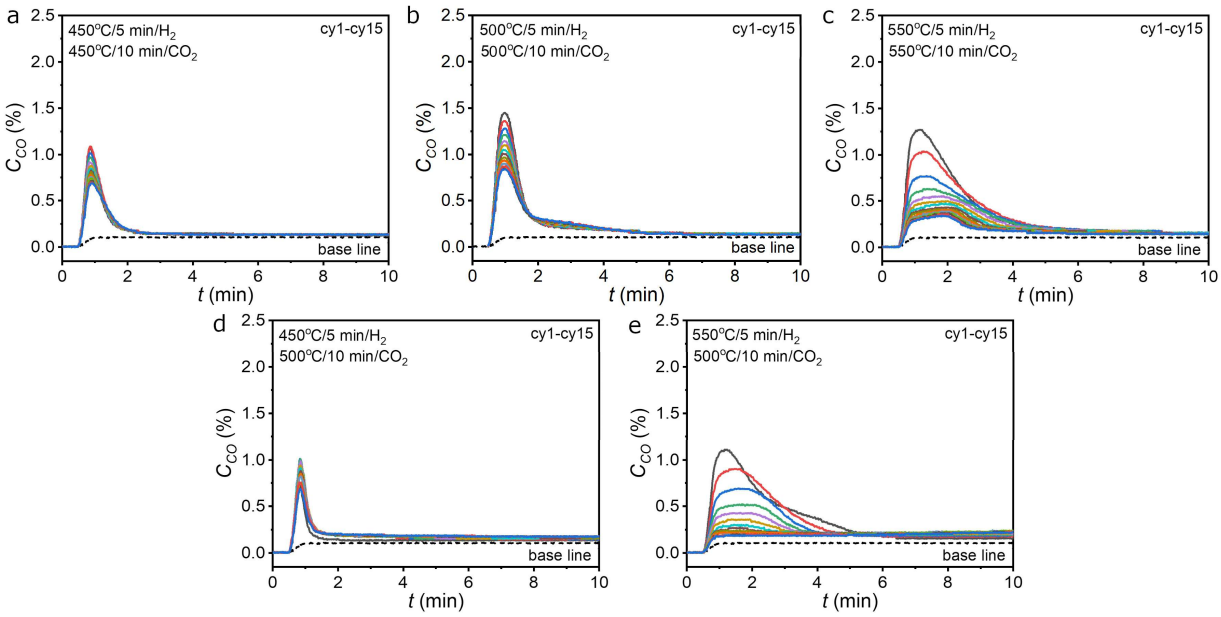

Figure S1. Recorded real-time CO concentration during chemical looping CO_2-splitting step with a H_2 / CO_2 program of 5 min / 10 min after different process temperatures. (a) H_2 / CO_2 = 450 °C / 450 °C, (b) H_2 / CO_2 = 500 °C / 500 °C, (c) H_2 / CO_2 = 550 °C / 550 °C, (d) H_2 / CO_2 = 450 °C / 500 °C and (e) H_2 / CO_2 = 550 °C / 500 °C. Condition: 300 sccm CO_2 (10% balanced with Ar), 300 sccm Ar (4N-grade), 300 sccm H_2 (5%, balanced with Ar).

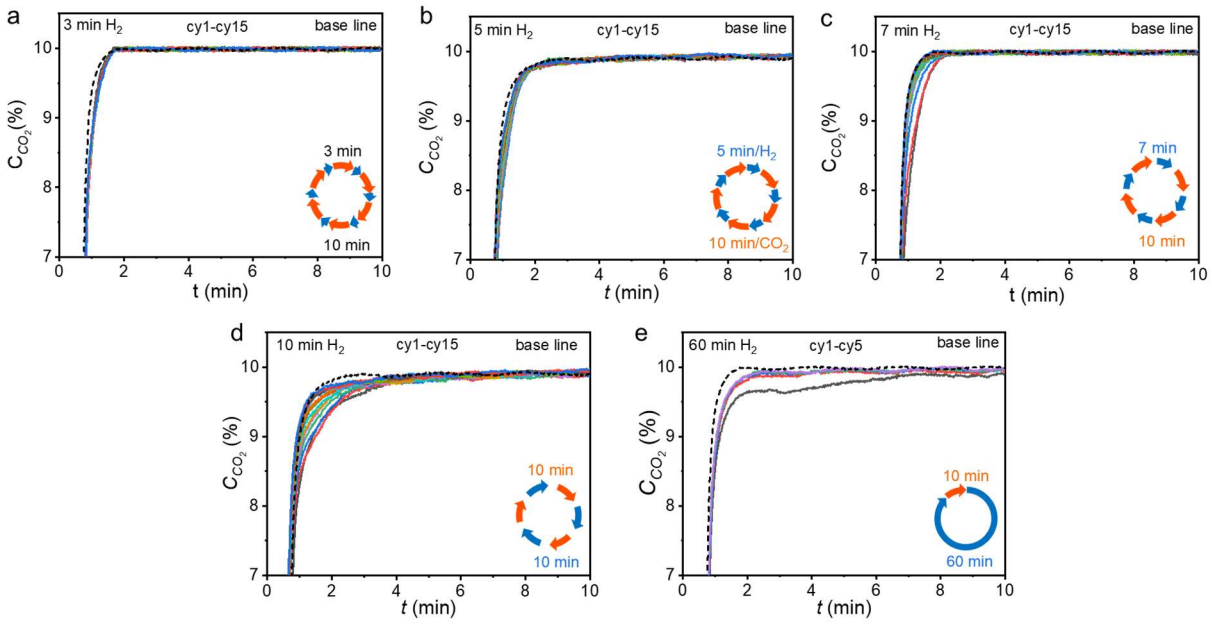

Figure S2. Recorded real-time CO_2 concentration during chemical looping CO_2-splitting step at 500 °C using Fe-oxygen carrier with different redox program. (a) H_2 / CO_2 = 3 min / 10 min, (b) H_2 / CO_2 = 5 min / 10 min, (c) H_2 / CO_2 = 7 min / 10 min, (d) H_2 / CO_2 = 10 min / 10 min, and (e) H_2 / CO_2 = 60 min / 10 min. Condition: 300 sccm CO_2 (10% balanced with Ar), 300 sccm Ar (4N-grade), 300 sccm H_2 (5%, balanced with Ar).

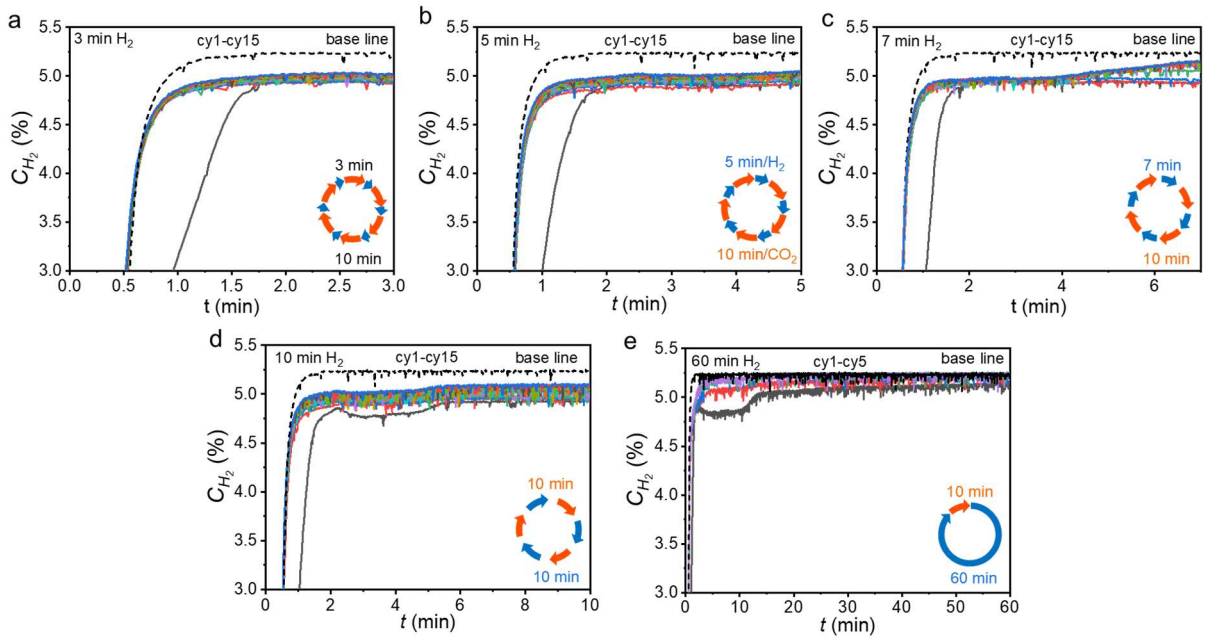

Figure S3. Recorded real-time H_2 concentration during chemical looping H_2-oxidation step at 500 °C using Fe-oxygen carrier with different redox program. (a) H_2 / CO_2 = 3 min / 10 min, (b) H_2 / CO_2 = 5 min / 10 min, (c) H_2 / CO_2 = 7 min / 10 min, (d) H_2 / CO_2 = 10 min / 10 min, and (e) H_2 / CO_2 = 60 min / 10 min. Condition: 300 sccm CO_2 (10% balanced with Ar), 300 sccm Ar (4N-grade), 300 sccm H_2 (5%, balanced with Ar).

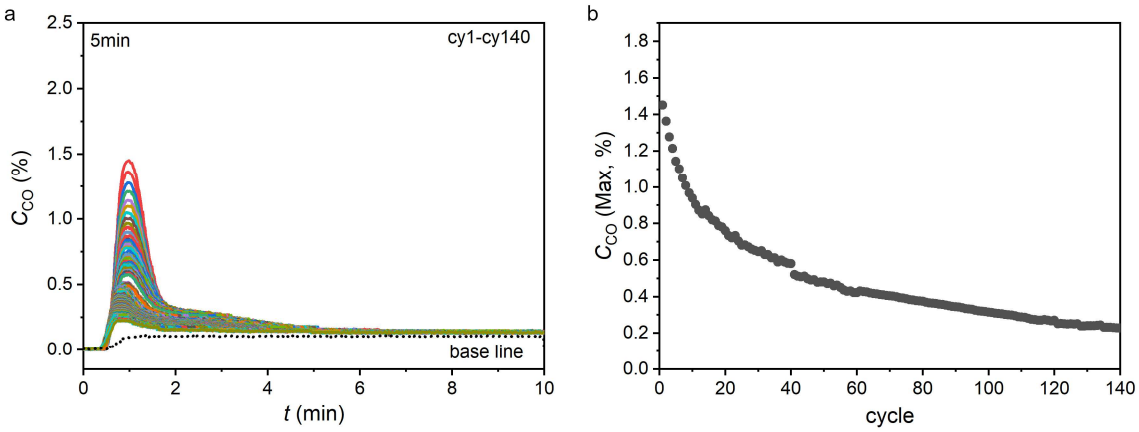

Figure S4. Stability of the 5 min / 10 min program over more than 100 cycles. (a) Recorded real-time CO concentration. (b) Maximum CO concentration recorded in each cycle.

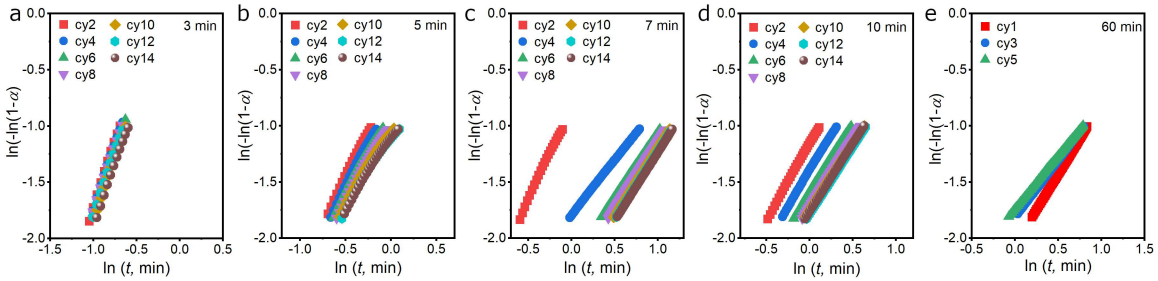

Figure S5. Plots of ln(-ln(1-a)) against ln(t) based on the data from Figure 2a-e.

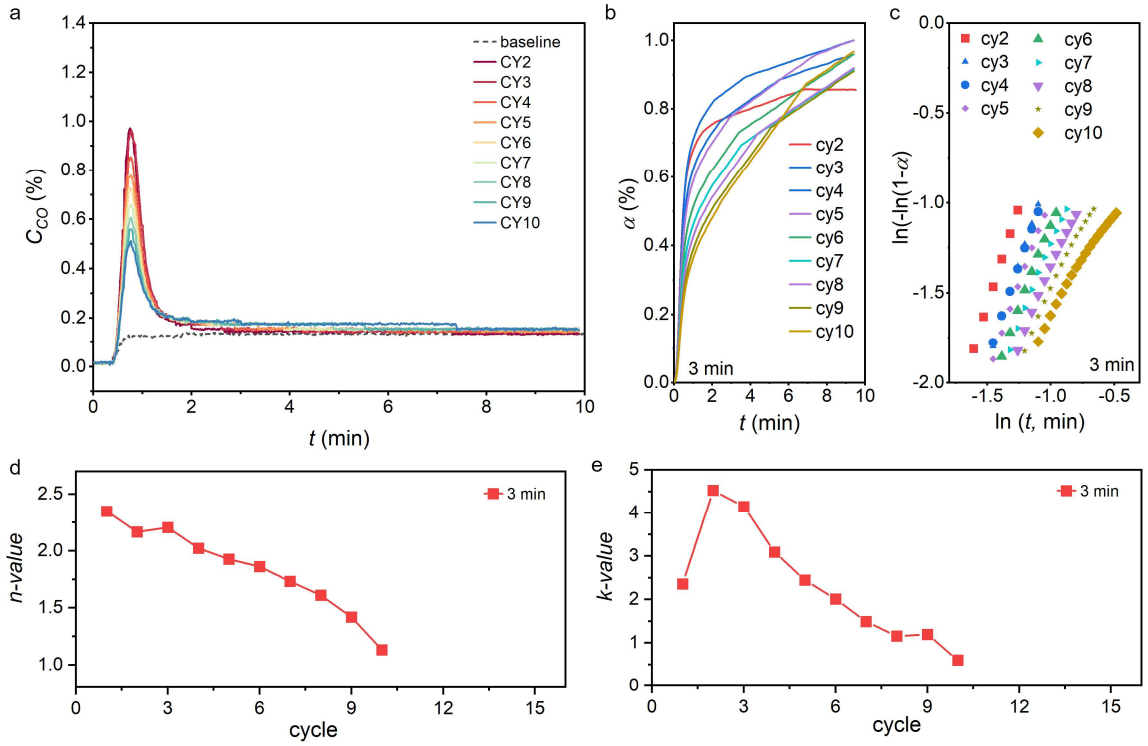

Figure S6. Repeated CL-RWGS using the 3 min / 10 min program. (a) Real-time CO concentration recorded by the NDIR, (b) a-t plot, (c) ln(-ln(1-a)) vs ln(t), (d) *n*-value, and (e) *k*-value over 10 cycles.

Supplementary Note 1: Smoothing of the raw CO_2-TPO data.

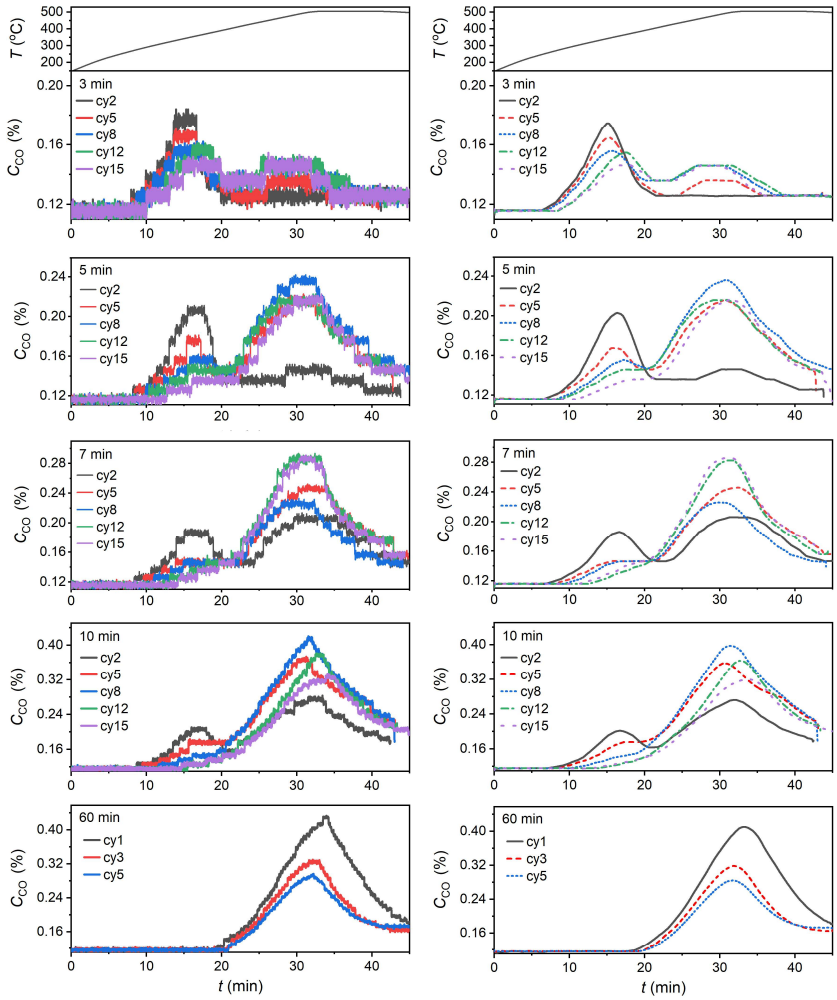

Figure S7. Raw and smoothed data of the CO_2 temperature programmed oxidation (CO_2-TPO) conducted on the iron oxygen carriers with increasing H_2 step duration from 3 min, 5 min, 7 min, 10 min, and 60 min (from top to bottom). The CO_2-TPO was conducted under 10 % CO_2 (balanced with Ar) from 150 °C with a ramp rate of 10 °C/min to 500 °C followed by a 15 min isothermal step. Other than the cycles listed in the legends, the CO_2 step was conducted under 500 °C for 10 min.

The smoothing of the CO_2-TPO data was conducted using the Origin software. The smoothed data presented in Figure 3a, 3d, 3g, 3j, and 3m was generated by performing adjacent-averaging

of the data presented in the left column of **Figure S7**, which consist of over 2500 data points. The points of window were set to 200 with no boundary conditions to average out the unrealistic steps in the raw data caused by the insufficient resolution of the NDIR detectors (**Figure S8**).

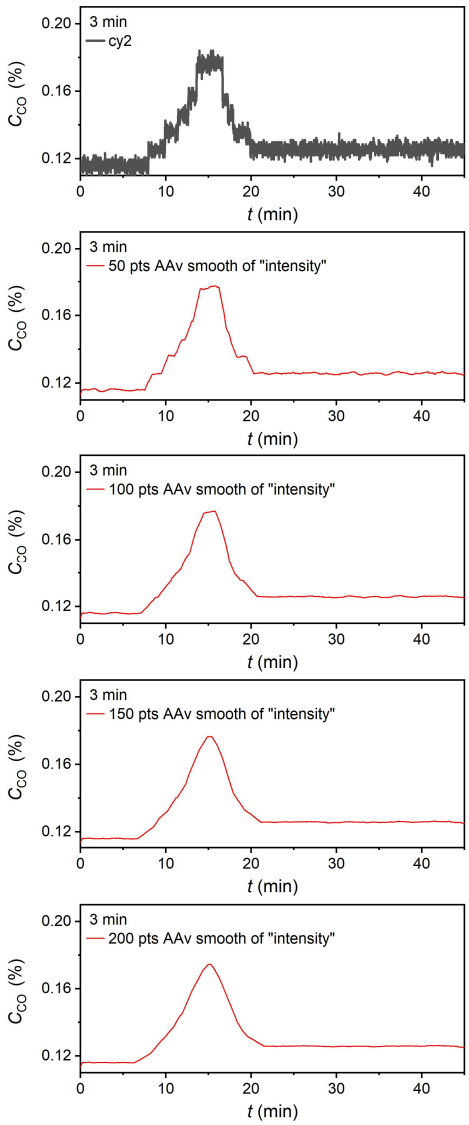

Figure S8. Raw and smoothed representative CO_2-TPO data with different points of windows.

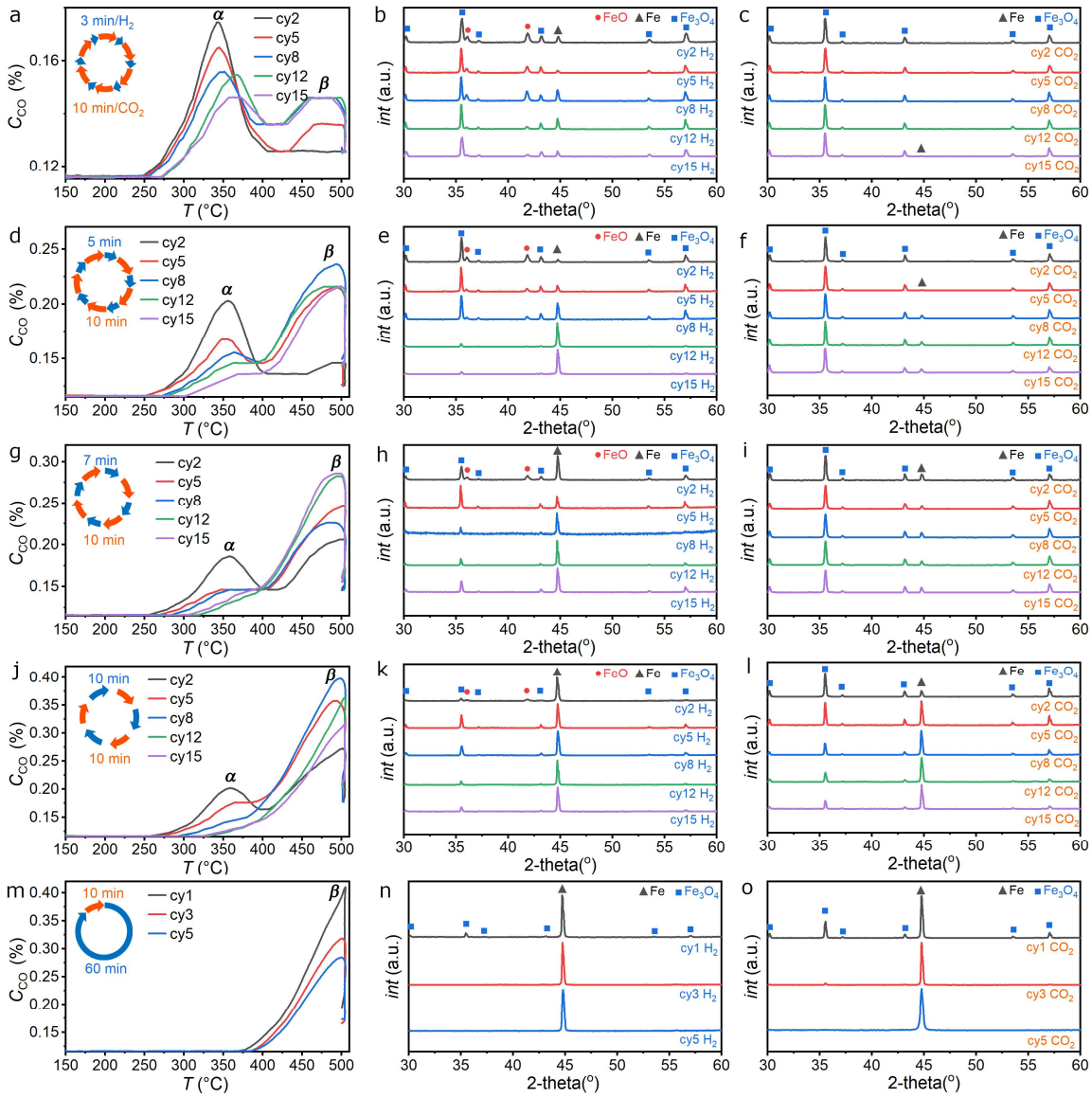

Figure S9. (a) CO_2-TPO profiles after selected cycles and corresponding PXRD patterns of the Fe oxygen carrier obtained after the (b) reduction and (c) oxidation step respectively using a H_2 / CO_2 program of 3 min / 10 min. Same type of data as presented in (a-c) except with a H_2 / CO_2 program of (d-f) 5 min / 10 min, (g-i) 7 min / 10 min, (j-l) 10 min / 10 min, and (m-o) 60 min / 10 min.

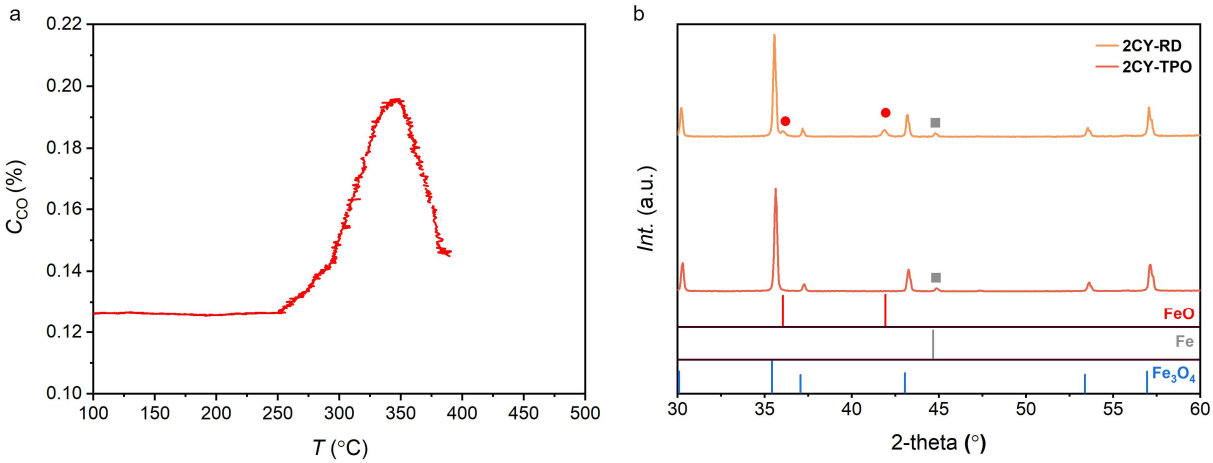

Figure S10. (a) CO concentration recorded during the CO_2-TPO cut-off after the first low-temperature α-peak. (b) PXRD pattern of the Fe oxygen carrier after the 2nd reduction step (2CY-RD) and quenched after the α-peak in the subsequent CO_2-TPO experiment (2CY-TPO).

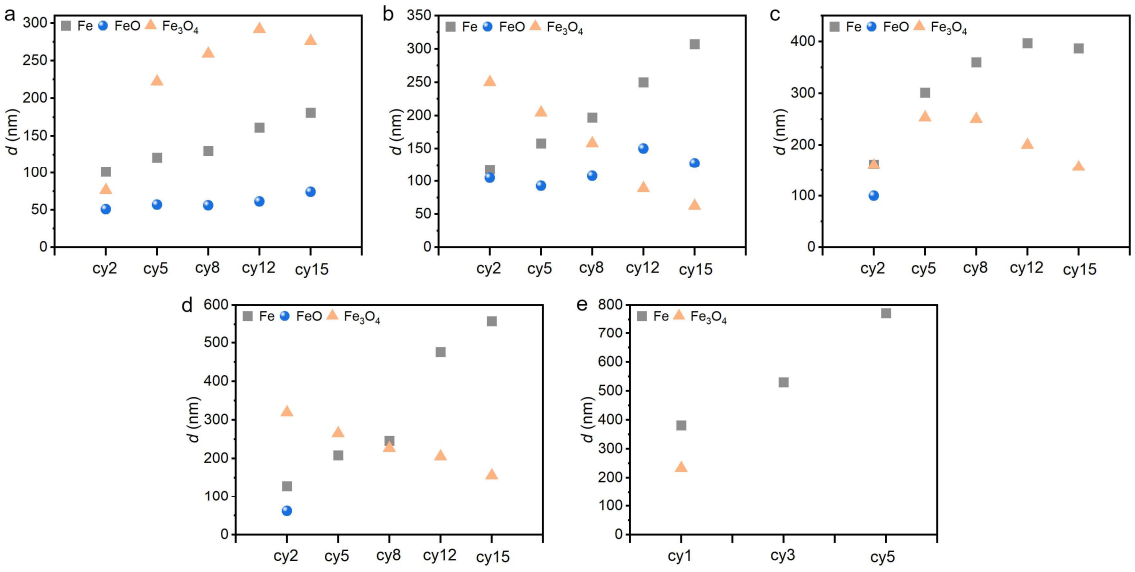

Figure S11. Grain size of Fe, FeO, and Fe_3O_4 of the Fe oxygen carrier obtained after reduction step using a H_2 / CO_2 program of (a) 3 min / 10 min, (b) 5 min / 10 min, (c) 7 min / 10 min, (d) 10 min / 10 min, and (e) 60 min / 10 min.

Table S1. Mole fraction and grain size of Fe, FeO, and Fe_3O_4 phases of the Fe-oxygen carriers obtained from the refinement of the PXRD patterns in Figure 3(b, e, h, k, n).

Sample	X_{Fe} (mol%)	d_{Fe} (nm)	X_{FeO} (mol%)	d_{FeO} (nm)	X_{Fe3O4} (mol%)	d_{Fe3O4} (nm)
3 min-cy2	6.1	101	40.8	51	53.1	76
3min-cy5	5.1	121	33.5	57	61.6	222
3min-cy8	21.6	130	27.8	56	50.6	259
3min-cy12	17.7	161	22.9	61	59.4	292
3min-cy15	16.8	181	15.7	74	67.5	276
5min-cy2	7.4	118	33.4	105	59.2	250
5min-cy5	12.9	158	14.7	93	72.4	204
5min-cy8	27.1	197	10.3	108	62.6	158
5min-cy12	74.8	250	3.3	150	21.9	89
5min-cy15	78.3	307	1.6	128	20.1	62
7min-cy2	16.1	162	39.0	100	44.9	160
7min-cy5	25.8	301	0	-	74.2	253
7min-cy8	58.3	360	0	-	41.7	250
7min-cy12	84.9	397	0	-	15.1	200
7min-cy15	81.9	387	0	-	18.1	156
10min-cy2	72.9	128	17.0	62	10.1	319
10min-cy5	54.8	208	0	-	45.2	265
10min-cy8	64.0	246	0	-	36.0	227
10min-cy12	87.3	476	0	-	12.8	205
10min-cy15	89.2	558	0	-	10.9	156
60min-cy1	86.2	381	0	-	13.8	233
60min-cy3	100	530	0	-	0	-
60min-cy5	100	772	0	-	0	-

Supplementary Note 2: Refinement of XRD Patterns by GSAS

The XRD quantitative analysis was conducted using GSAS-II software, employing the Rietveld full-pattern fitting method for peak fitting. Initially, the analysis file was imported by selecting the appropriate powder data format, such as “Topas xye” or “2th Fit2D chi file”. The instrument parameter file was then selected to ensure accurate analysis. Phases required for the analysis were added by importing from the CIF file, sourced from the ICSD database. To correct the position of each phase, lattice constants were adjusted within the phase's general settings, ensuring that the reference positions aligned with the experimental data. Once aligned, the lattice constants were fixed to maintain consistency. Constraints were applied to ensure that the sum of all phase proportions equaled 1, maintaining the overall balance in the quantitative analysis. Subsequently, phase fractions were analyzed by adjusting them to match the experimental data. Once a match was achieved, these parameters were fixed. The grain size (nm) of each phase was analyzed next, where an initial refinement was performed to adjust the peak shape to closely resemble the experimental data, followed by fixing this parameter. This process was repeated for all phases under the present study. The final output included the proportions of each phase and grain size, providing a comprehensive quantitative analysis of the sample. The snapshots of the fitting results for all patterns presented are provided below:

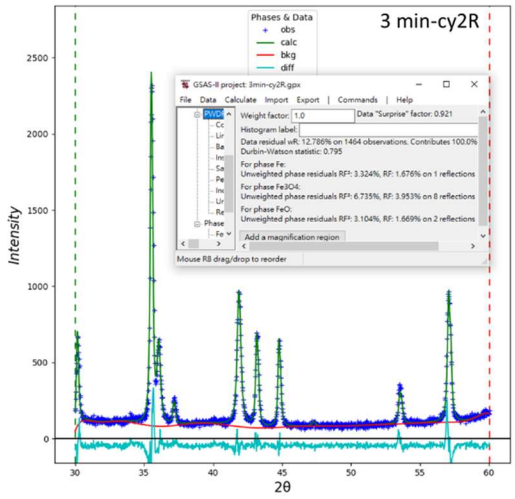
3 min-cy2R
Phases & Data
obs
calc
bkg
diff
Intensity
2θ

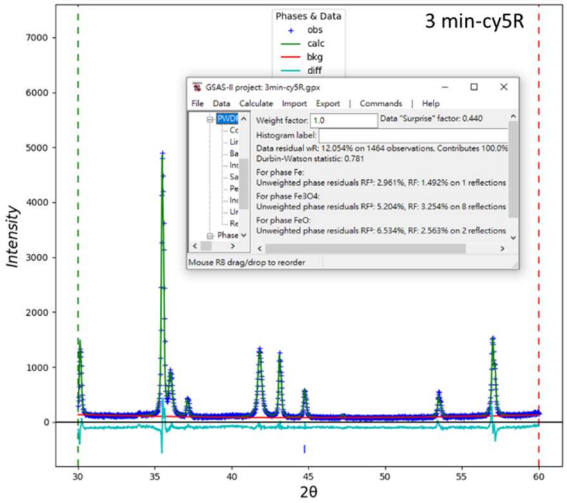
3 min-cy5R
Phases & Data
obs
calc
bkg
diff
Intensity
2θ

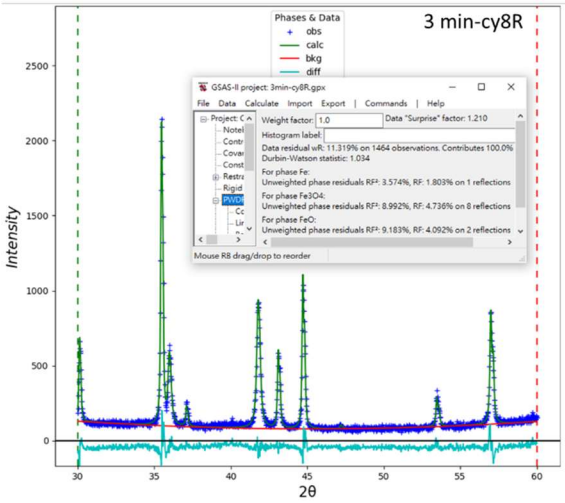
3 min-cy8R
Phases & Data
obs
calc
bkg
diff
Intensity
2θ

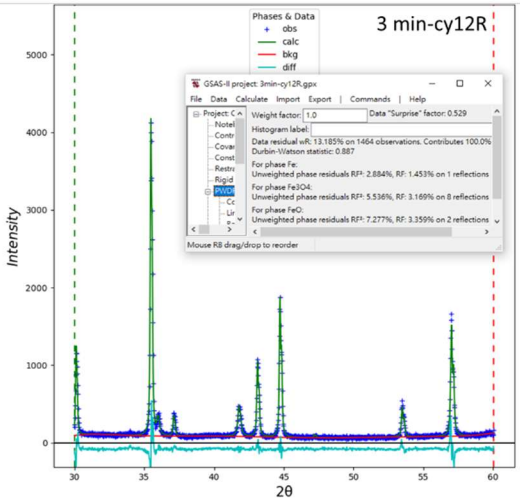
3 min-cy12R
Phases & Data
obs
calc
bkg
diff
Intensity
2θ

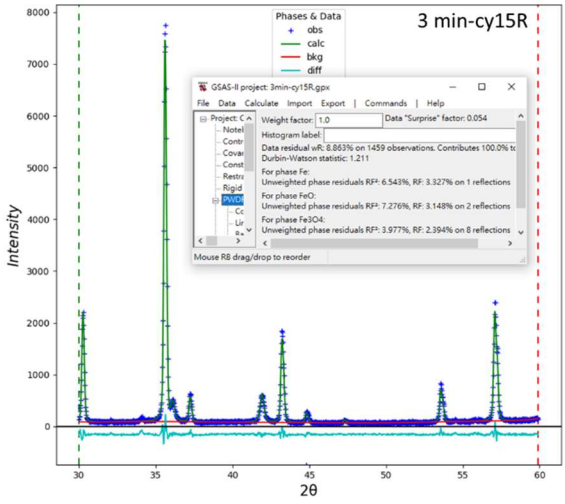
3 min-cy15R
Phases & Data
obs
calc
bkg
diff
Intensity
2θ

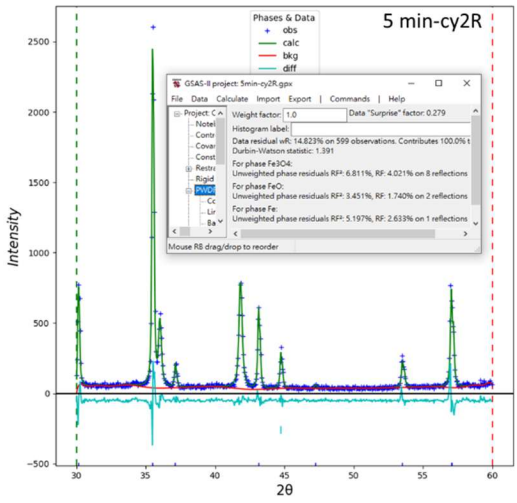
5 min-cy2R
Phases & Data
obs
calc
bkg
diff
GSAS-II project: 5min-cy2R.gpx
Weight factor: 1.0
Data "Surprise" factor: 0.279
Intensity
2θ

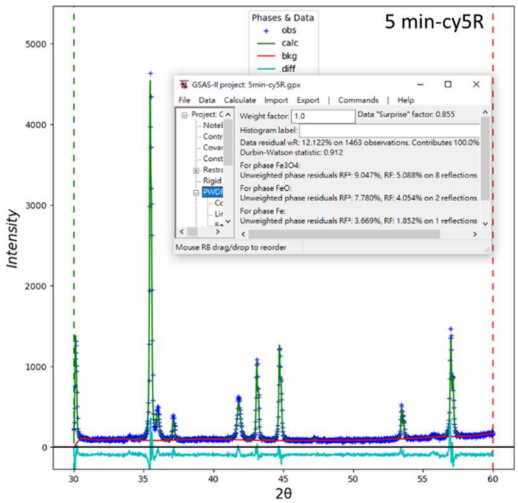
5 min-cy5R
Phases & Data
obs
calc
bkg
diff
GSAS-II project: 5min-cy5R.gpx
Weight factor: 1.0
Data "Surprise" factor: 0.855
Intensity
2θ

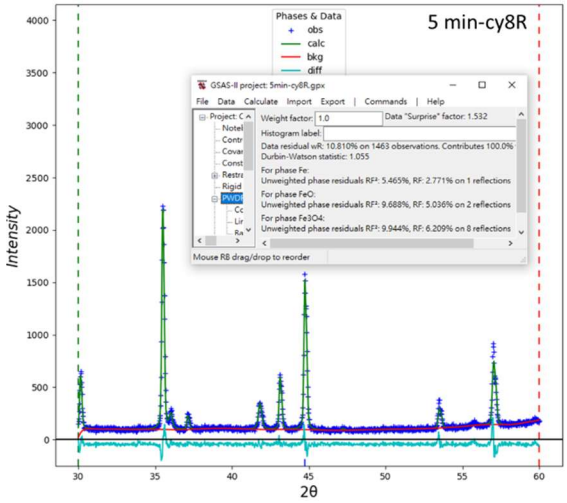
5 min-cy8R
Phases & Data
obs
calc
bkg
diff
GSAS-II project: 5min-cy8R.gpx
Weight factor: 1.0
Data "Surprise" factor: 1.532
Intensity
2θ

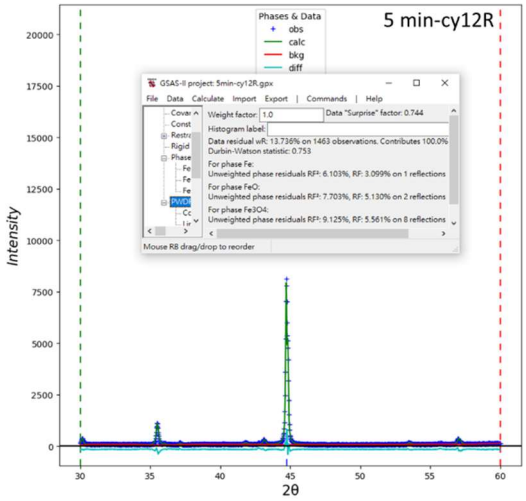
5 min-cy12R
Phases & Data
obs
calc
bkg
diff
GSAS-II project: 5min-cy12R.gpx
Weight factor: 1.0
Data "Surprise" factor: 0.744
Intensity
2θ

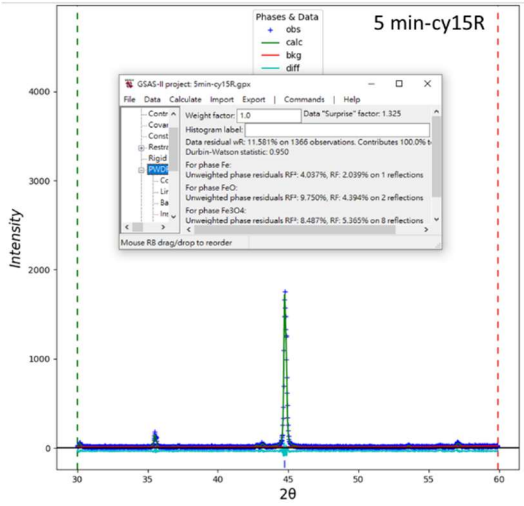
5 min-cy15R
Phases & Data
obs
calc
bkg
diff
GSAS-II project: 5min-cy15R.gpx
Weight factor: 1.0
Data "Surprise" factor: 1.325
Intensity
2θ

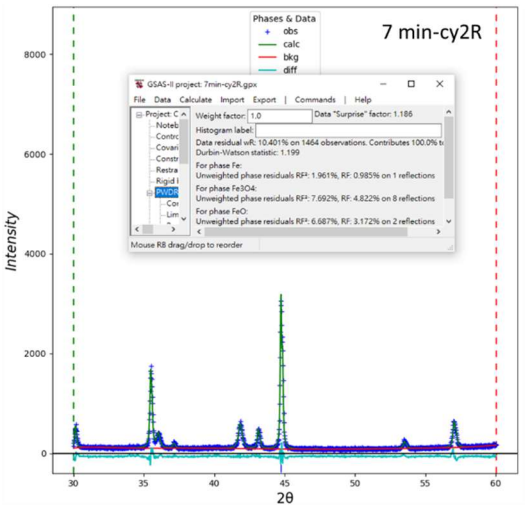
7 min-cy2R
Phases & Data
obs
calc
bkg
diff
GSAS-II project: 7min-cy2R.gpx
Intensity
2θ

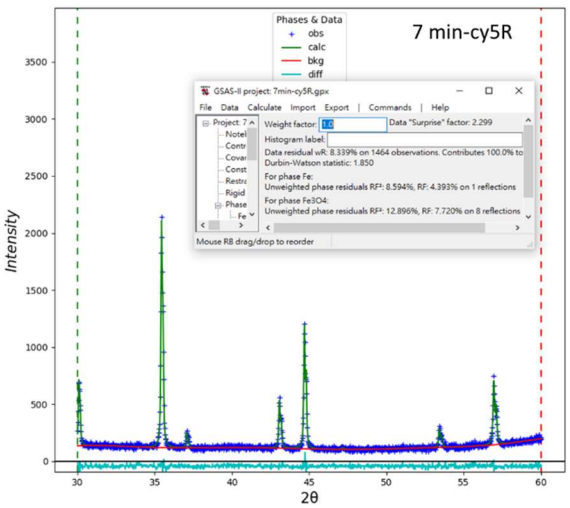
7 min-cy5R
Phases & Data
obs
calc
bkg
diff
GSAS-II project: 7min-cy5R.gpx
Intensity
2θ

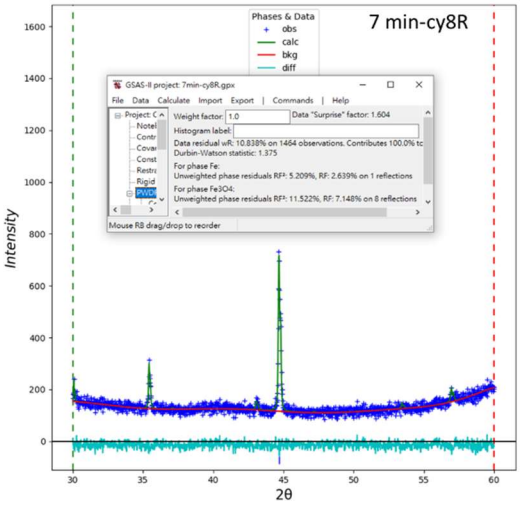
7 min-cy8R
Phases & Data
obs
calc
bkg
diff
GSAS-II project: 7min-cy8R.gpx
Intensity
2θ

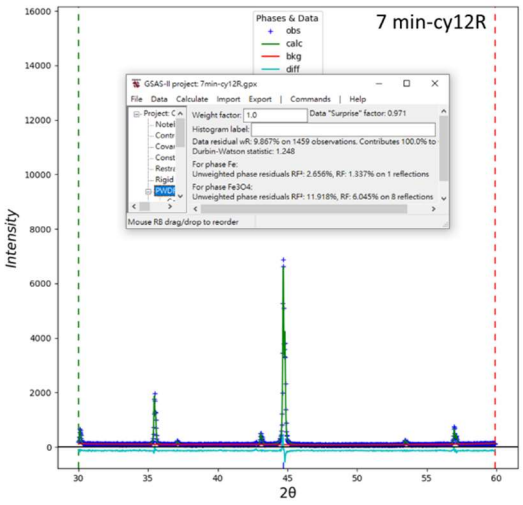
7 min-cy12R
Phases & Data
obs
calc
bkg
diff
GSAS-II project: 7min-cy12R.gpx
Intensity
2θ

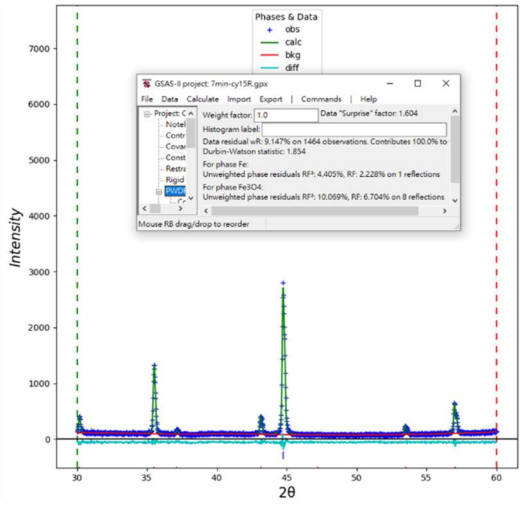
Phases & Data
obs
calc
bkg
diff
GSAS-II project: 7min-cy15R.gpx
Intensity
2θ

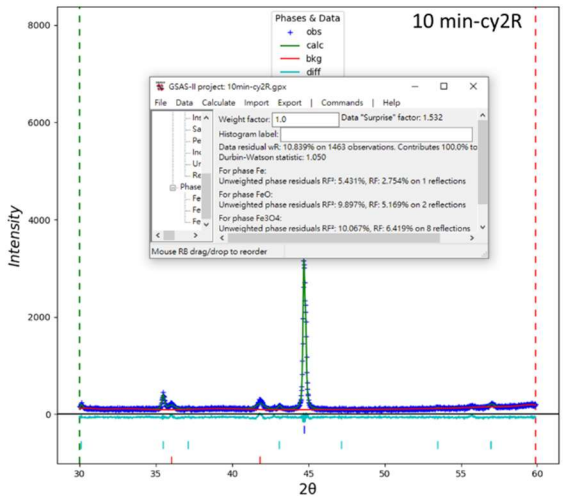
10 min-cy2R
Phases & Data
obs
calc
bkg
diff
GSAS-II project: 10min-cy2R.gpx
File Data Calculate Import Export | Commands | Help
Weight factor: 1.0
Data "Surprise" factor: 1.532
Histogram label:
Data residual wR: 10.839% on 1463 observations. Contributes 100.0% to
Durbin-Watson statistic: 1.050
For phase Fe:
Unweighted phase residuals RF²: 5.431%, RF: 2.754% on 1 reflections
For phase FeO:
Unweighted phase residuals RF²: 9.897%, RF: 5.169% on 2 reflections
For phase Fe3O4:
Unweighted phase residuals RF²: 10.067%, RF: 6.419% on 8 reflections
Mouse RB drag/drop to reorder
Intensity
2θ

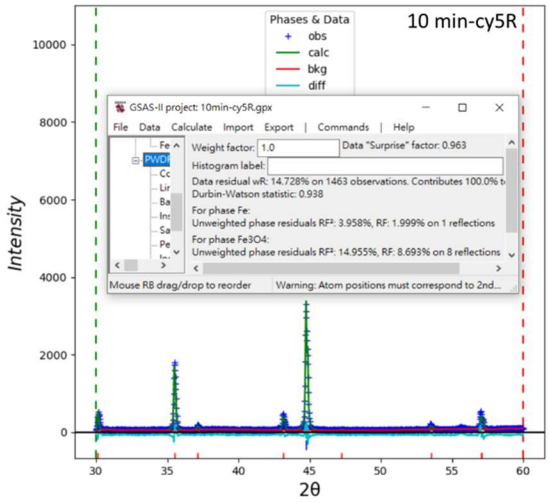
10 min-cy5R
Phases & Data
obs
calc
bkg
diff
GSAS-II project: 10min-cy5R.gpx
File Data Calculate Import Export | Commands | Help
Weight factor: 1.0
Data "Surprise" factor: 0.963
Histogram label:
Data residual wR: 14.728% on 1463 observations. Contributes 100.0% t
Durbin-Watson statistic: 0.938
For phase Fe:
Unweighted phase residuals RF²: 3.958%, RF: 1.999% on 1 reflections
For phase Fe3O4:
Unweighted phase residuals RF²: 14.955%, RF: 8.693% on 8 reflections
Mouse RB drag/drop to reorder
Warning: Atom positions must correspond to 2nd...
Intensity
2θ

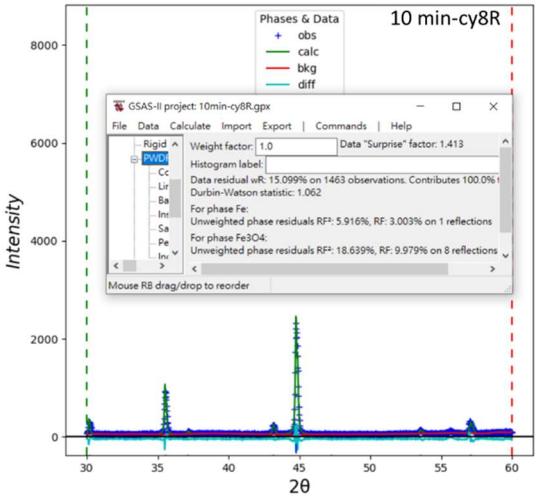
10 min-cy8R
Phases & Data
obs
calc
bkg
diff
GSAS-II project: 10min-cy8R.gpx
File Data Calculate Import Export | Commands | Help
Weight factor: 1.0
Data "Surprise" factor: 1.413
Histogram label:
Data residual wR: 15.099% on 1463 observations. Contributes 100.0%
Durbin-Watson statistic: 1.062
For phase Fe:
Unweighted phase residuals RF²: 5.916%, RF: 3.003% on 1 reflections
For phase Fe3O4:
Unweighted phase residuals RF²: 18.639%, RF: 9.979% on 8 reflections
Mouse RB drag/drop to reorder
Intensity
2θ

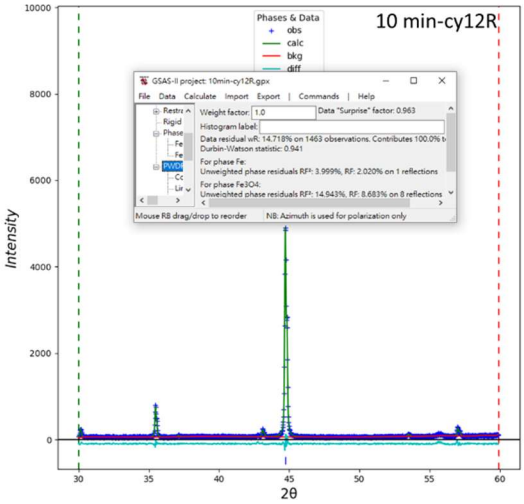
10 min-cy12R
Phases & Data
obs
calc
bkg
diff
GSAS-II project: 10min-cy12R.gpx
File Data Calculate Import Export | Commands | Help
Weight factor: 1.0
Data "Surprise" factor: 0.963
Histogram label:
Data residual wR: 14.718% on 1463 observations. Contributes 100.0%
Durbin-Watson statistic: 0.941
For phase Fe:
Unweighted phase residuals RF²: 3.999%, RF: 2.020% on 1 reflections
For phase Fe3O4:
Unweighted phase residuals RF²: 14.943%, RF: 8.683% on 8 reflections
Mouse RB drag/drop to reorder
NB: Azimuth is used for polarization only
Intensity
2θ

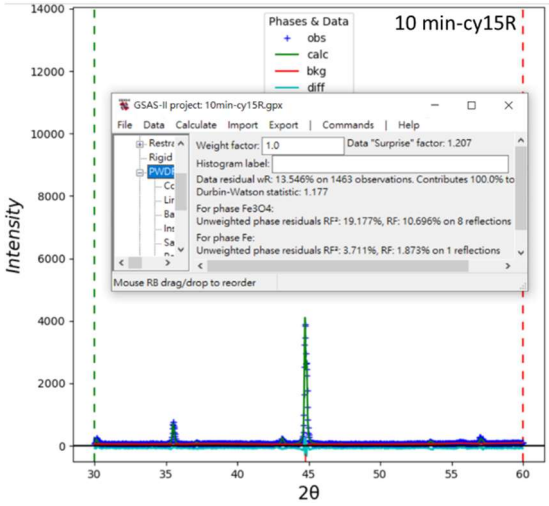
10 min-cy15R
Phases & Data
obs
calc
bkg
diff
GSAS-II project: 10min-cy15R.gpx
File Data Calculate Import Export | Commands | Help
Weight factor: 1.0
Data "Surprise" factor: 1.207
Histogram label:
Data residual wR: 13.546% on 1463 observations. Contributes 100.0% to
Durbin-Watson statistic: 1.177
For phase Fe3O4:
Unweighted phase residuals RF²: 19.177%, RF: 10.696% on 8 reflections
For phase Fe:
Unweighted phase residuals RF²: 3.711%, RF: 1.873% on 1 reflections
Mouse RB drag/drop to reorder
Intensity
2θ

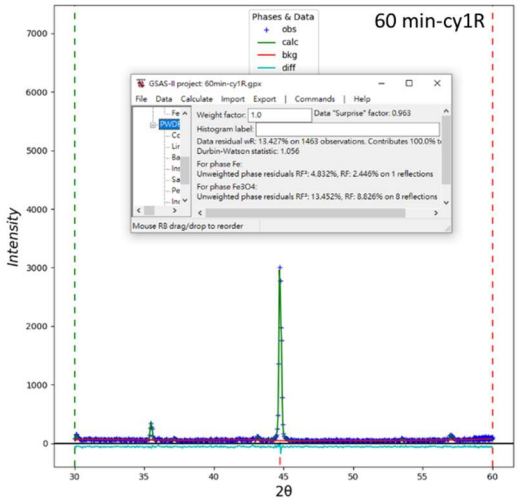
60 min-cy1R
Phases & Data
obs
calc
bkg
diff
GSAS-II project: 60min-cy1R.gpx
File Data Calculate Import Export | Commands | Help
Weight factor: 1.0
Data "Surprise" factor: 0.963
Histogram label:
Data residual wR: 13.427% on 1463 observations. Contributes 100.0% t
Durbin-Watson statistic: 1.056
For phase Fe:
Unweighted phase residuals RF²: 4.832%, RF: 2.446% on 1 reflections
For phase Fe3O4:
Unweighted phase residuals RF²: 13.452%, RF: 8.826% on 8 reflections
Mouse RB drag/drop to reorder
Intensity
2θ

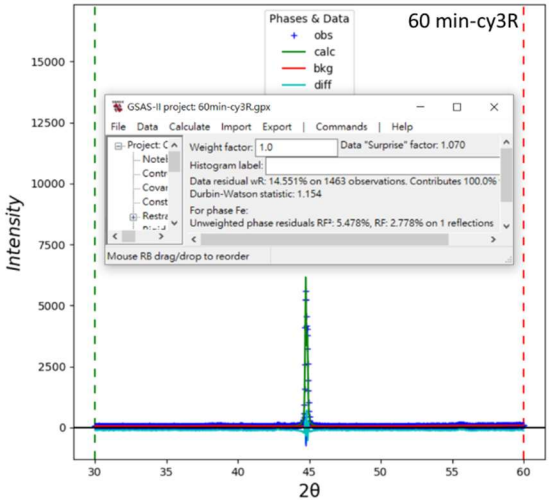
60 min-cy3R
Phases & Data
obs
calc
bkg
diff
GSAS-II project: 60min-cy3R.gpx
File Data Calculate Import Export | Commands | Help
Weight factor: 1.0
Data "Surprise" factor: 1.070
Histogram label:
Data residual wR: 14.551% on 1463 observations. Contributes 100.0%
Durbin-Watson statistic: 1.154
For phase Fe:
Unweighted phase residuals RF²: 5.478%, RF: 2.778% on 1 reflections
Mouse RB drag/drop to reorder
Intensity
2θ

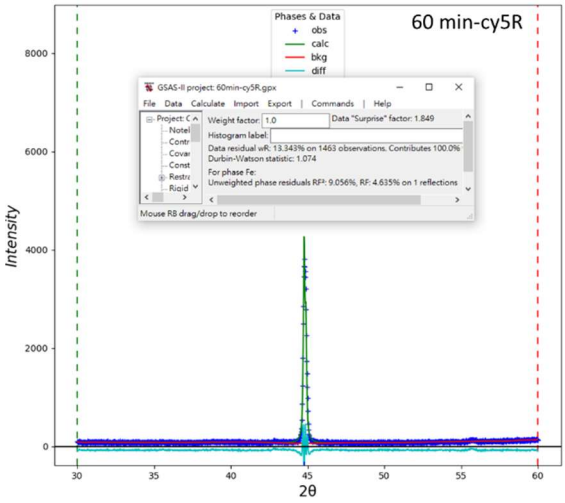
60 min-cy5R
Phases & Data
obs
calc
bkg
diff
GSAS-II project: 60min-cy5R.gpx
File Data Calculate Import Export | Commands | Help
Weight factor: 1.0
Data "Surprise" factor: 1.849
Histogram label:
Data residual wR: 13.343% on 1463 observations. Contributes 100.0%
Durbin-Watson statistic: 1.074
For phase Fe:
Unweighted phase residuals RF²: 9.056%, RF: 4.635% on 1 reflections
Mouse RB drag/drop to reorder
Intensity
2θ

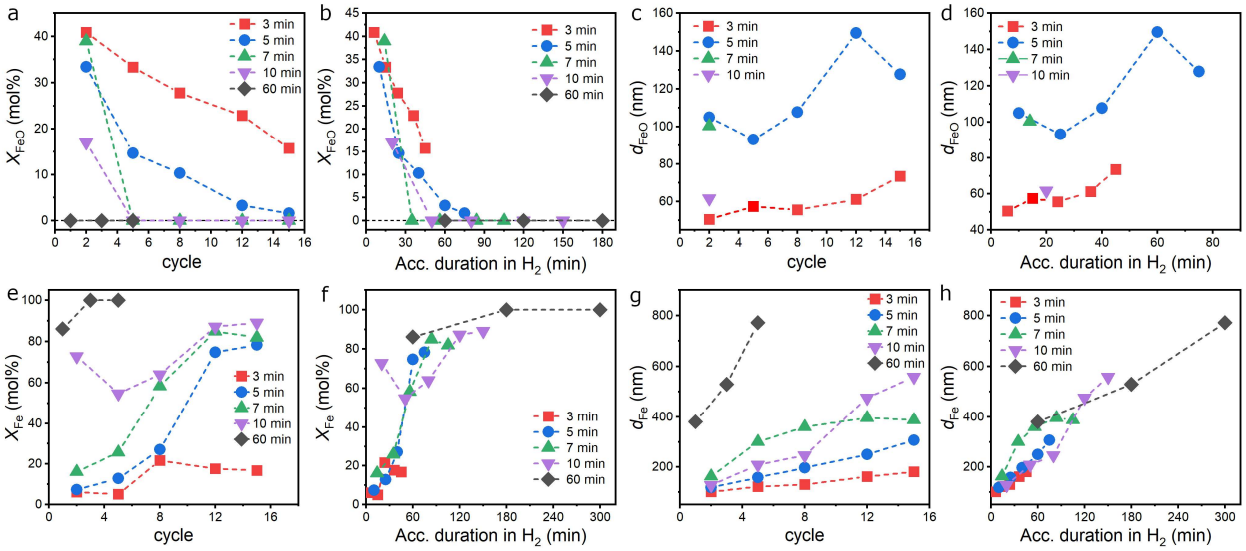

Figure S12. Graphical summary of the mole fraction and grain size of Fe and FeO in the oxygen carrier. (a, b) Mole fraction of FeO, (c, d) grain size of FeO, (e, f) mole fraction of Fe, and (g, h) grain size of Fe plotted over the number of looping cycles and the accumulated duration in H_2.

Notes: In general, the FeO content was higher in each cycle for programs with shorter H_2 steps (**Figure S12a**). However, the 3 min / 10 min program remains unique as it preserved significantly more FeO even treated with the same amount of H_2 accumulatively (**Figure S12b**). The growth in FeO grain size was also inhibited with more frequent cycling, being maintained below 80 nm for the 3 min / 10 min program while increased above 120 nm for the 5 min / 10 min program (**Figure S12c, d**). On the contrary, Fe content was higher for programs with longer H_2 steps and became the dominant phase (**Figure S12e, f**). The grain size of Fe in the oxygen carriers increased with increasing number of cycles (**Figure S12g**) and the accumulated duration in H_2 (**Figure S12h**). The size of the Fe grains was typically 2~3 times larger than FeO and can exceed 500 nm for long H_2-steps. The 7 min / 10 min program was a special exception where the grain size of Fe reached a stable level around 400 nm. This explained its slow but persistent CO_2-splitting ability.

Supplementary Note 3: The computational benchmark for FeO

We varied the effective Hubbard U parameter from 0 to 6 eV and identified U = 3.7 eV as optimal for reproducing the electronic and structural properties of bulk FeO (**Figure S13a**), consistent with the prior work of Peilin Liao and Emily A. Carter [1]. With this setup, the calculated electronic band gap (E_{gap}) is 1.29 eV. Orbital-resolved analysis indicates that this gap is governed by transitions into the Fe 4s manifold. Specifically, the first unoccupied Fe 4s state appears at ~1.29 eV above the Fermi level and marks the onset of the conduction band (**Figure S13b**). This result is consistent with the DFT study by Mazin et al., who reported a minimum gap of ~1.3 eV [2]. As noted by T. Eom et al., the primary role of U in FeO is to tune the magnitude of the computed E_{gap} [3]. The selected value, U = 3.7 eV, lies within the commonly used 3–5 eV range for FeO [4–8].

It is important to distinguish the calculated electronic band gap from optical absorption features reported experimentally. The stronger optical edge observed near ~2.4 eV is commonly attributed to transitions into Fe 3d states [9–11]. In our projected density of states (PDOS) calculations, the first unoccupied Fe 3d peak appears at ~2.8 eV above the Fermi level. While this is somewhat higher than the upper end of the experimental optical edge (~2.4 eV), it remains within an acceptable range for the present benchmarking purpose. Using larger U values would shift the unoccupied states to higher energies and further increase the deviation from the experimental spectroscopic features.

The reliability of this electronic description also depends on including both antiferromagnetic (AFM) ordering and spin–orbit coupling (SOC), which are critical for maintaining the insulating character of FeO in our calculations (**Figure S13c** and **Table S2**). As reported by Forti et al., SOC can lift the degeneracy of Fe d-orbital states near the Fermi level, particularly the t_{2g} manifold, an effect that may not be captured adequately by GGA+ U alone [12]. Table S2 compares the predicted

bulk properties for ferromagnetic (FM) and AFM orderings, highlighting the combined impact of the Hubbard correction and SOC. With the selected settings, we obtain an Fe–O bond length $l_{Fe\text{-}O}$ = 2.19 Å, corresponding to a lattice parameter a = 4.38 Å for the Fm3m structure. This value is close to the experimental lattice parameter of 4.34 Å [13] (**Figure S13d**). The projected magnetic moment on Fe is $\mu_{Fe} = \pm 3.74\ \mu_B$. Overall, these results are consistent with established experimental and theoretical benchmarks [14–21].

Table S2. Structural and electronic properties of FeO bulk phases under various magnetic and computational considerations. The settings ultimately adopted in this study are highlighted in bold.

System	Magnetism	U_{eff} (eV)	SOC	a (Å)	$l_{Fe\text{-}O}$ (Å)	μ_{Fe} (μ_B)	E_{gap} (eV)
FeO bulk	FM	0	no	4.310	2.155	3.620	metallic
	AFM	0	no	4.321	2.161	±3.545	metallic
	FM	3.7	no	4.307	2.153	3.796	metallic
	AFM	3.7	no	4.378	2.189	±3.739	metallic
	FM	0	yes	4.310	2.155	3.616	metallic
	AFM	0	yes	4.321	2.161	±3.541	metallic
	FM	3.7	yes	4.390	2.195	3.742	metallic
	AFM	**3.7**	**yes**	**4.380**	**2.190**	**±3.737**	**1.288**

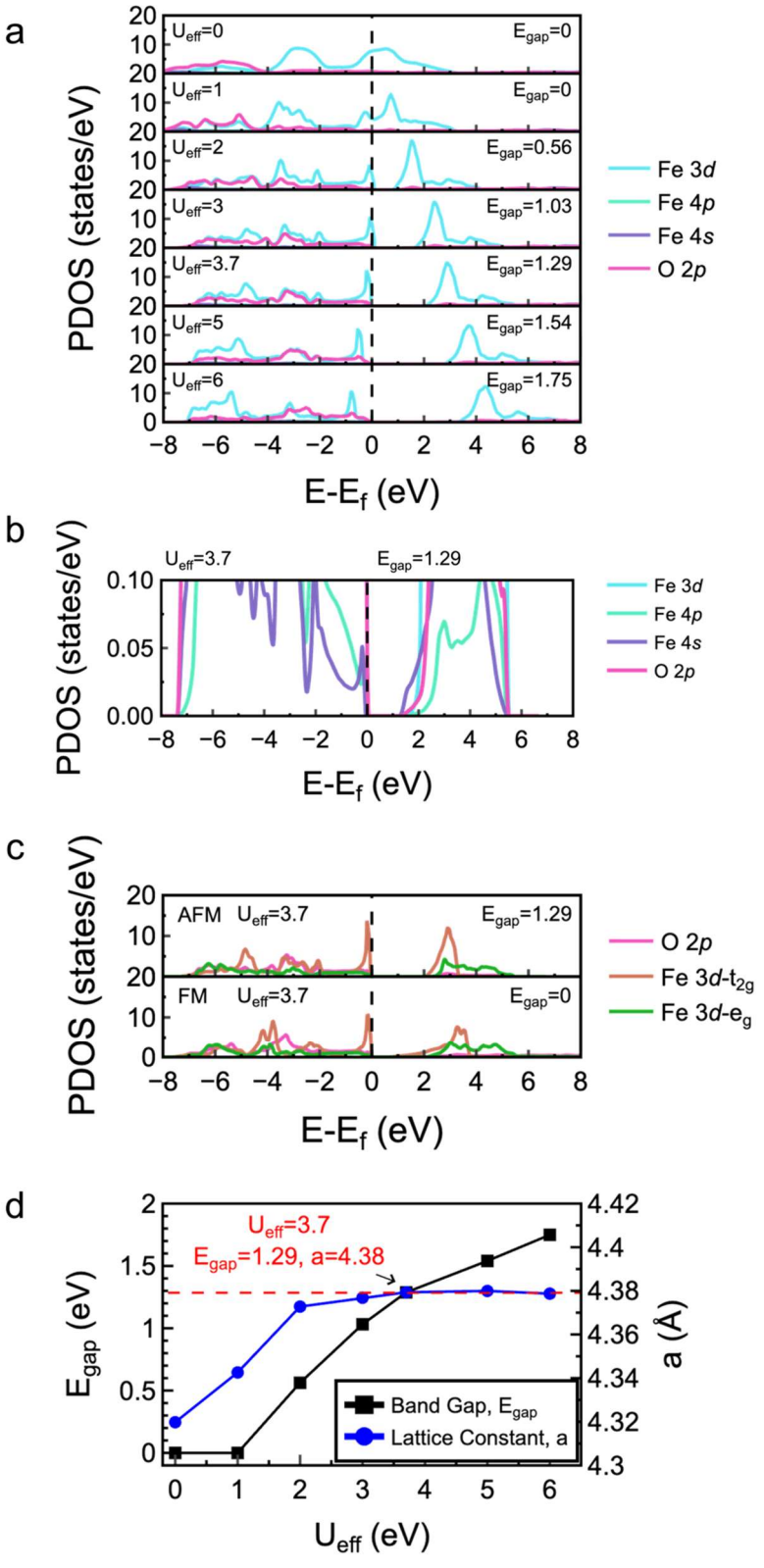
a
PDOS (states/eV)
E-E$_f$ (eV)
U$_{eff}$=0
E$_{gap}$=0
U$_{eff}$=1
E$_{gap}$=0
U$_{eff}$=2
E$_{gap}$=0.56
U$_{eff}$=3
E$_{gap}$=1.03
U$_{eff}$=3.7
E$_{gap}$=1.29
U$_{eff}$=5
E$_{gap}$=1.54
U$_{eff}$=6
E$_{gap}$=1.75
Fe 3d
Fe 4p
Fe 4s
O 2p
b
PDOS (states/eV)
E-E$_f$ (eV)
U$_{eff}$=3.7
E$_{gap}$=1.29
Fe 3d
Fe 4p
Fe 4s
O 2p
c
PDOS (states/eV)
E-E$_f$ (eV)
AFM U$_{eff}$=3.7
E$_{gap}$=1.29
FM U$_{eff}$=3.7
E$_{gap}$=0
O 2p
Fe 3d-t$_{2g}$
Fe 3d-e$_g$
d
E$_{gap}$ (eV)
a (Å)
U$_{eff}$ (eV)
U$_{eff}$=3.7
E$_{gap}$=1.29, a=4.38
Band Gap, E$_{gap}$
Lattice Constant, a

Figure S13. Benchmarking of the Hubbard U_{eff} parameter for bulk FeO via non-collinear SOC calculations. (a) Evolution of the PDOS under the AFM configuration as a function of the Hubbard U parameter (U_{eff} = 0 to 6 eV), benchmarking the sensitivity of the electronic band gap (E_{gap}) to the U value. (b) Magnified view of the PDOS near the Fermi level for the AFM case (U_{eff} = 3.7 eV). (c) Comparison between ferromagnetic (FM) and antiferromagnetic (AFM) spin configurations, both calculated at a Hubbard U parameter of U_{eff} = 3.7 eV. (d) Impact of the Hubbard U_{eff} parameter on the FeO lattice constant (a) and electronic band gap (E_{gap}). The red dashed line denotes the final settings adopted in this work.

Supplementary Note 4: Surface cleavage and magnetism

To enable a rational comparison between Fe and FeO surfaces, low-index facets (such as (100), (110), and (111)) of both materials were investigated (see **Table S3**). For Fe, only the ferromagnetic configuration was considered, excluding Hubbard U or SOC corrections as the standard PBE functional alone is sufficient to accurately reproduce the fundamental properties of this material. [24–26] For FeO, various magnetic orderings (AFM vs. FM) and corrections—including Hubbard U and SOC—were also considered. Ultimately, the energetically most favorable FeO (100) and Fe (100) facets were selected for subsequent calculations, exhibiting surface energies (E_s/A) of 0.037 and 0.153 eV/Å², respectively.

The surface formation energies (E_s) were calculated using **Eq. S1**, where E_* represents the total energy of the cleaved slab, n is the number of atoms in the slab, E_{bulk} denotes the energy per atom in bulk phases, and A is the surface area of each unit cell.

$$E_s = \frac{1}{2A}(E_* - n \cdot E_{bulk}) \qquad \textbf{Eq. S1}$$

Table S3. Energetics of low-index Fe and FeO facets. Surface formation energies per unit area (E_s/A) evaluated under varying correction schemes and spin configurations, with each calculation employing its own relaxed lattice. To simplify the calculations of FeO facets, the slab models were initialized using lattice parameters obtained from AFM- and FM-relaxed bulk structures for $U_{eff} \neq 0$ and $U_{eff} = 0$ cases, respectively. Bolded entries denote the selected facet and conditions for the calculations of reaction energy pathway.

Surface	Magnetism	U_{eff} (eV)	SOC	E_s (eV)	A (Å²)	E_s/A (eV/Å²)
Fe(100)	**FM**	**0**	**no**	**4.906**	**32.103**	**0.153**
Fe(110)	FM	0	no	3.526	22.700	0.155
Fe(111)	FM	0	no	9.003	55.604	0.162
FeO(100)	**AFM**	**3.7**	**yes**	**0.703**	**19.184**	**0.037**
	AFM	3.7	no	3.087	19.171	0.161
	AFM	0	yes	1.857	18.572	0.100
	AFM	0	no	1.857	18.575	0.100
	FM	3.7	yes	1.282	19.184	0.067
	FM	3.7	no	2.902	19.171	0.151
	FM	0	yes	0.525	18.572	0.028
	FM	0	no	0.523	18.575	0.028
FeO(110)	AFM	3.7	yes	1.739	27.131	0.064
	AFM	3.7	no	1.678	27.112	0.062
	AFM	0	yes	1.586	26.265	0.060
	AFM	0	no	1.584	26.269	0.060
	FM	3.7	yes	1.978	27.131	0.073
	FM	3.7	no	2.918	27.112	0.108
	FM	0	yes	1.713	26.265	0.065
	FM	0	no	1.713	26.269	0.065
FeO(111)	AFM	3.7	yes	3.522	33.228	0.106

AFM	3.7	no	3.332	33.205	0.100
AFM	0	yes	1.837	32.168	0.057
AFM	0	no	1.833	32.172	0.057
FM	3.7	yes	4.198	33.228	0.126
FM	3.7	no	5.541	33.205	0.167
FM	0	yes	2.833	32.168	0.088
FM	0	no	2.835	32.172	0.088

It is worth highlighting, as reported by S. Yoon *et al*., that the potential energy surface of magnetic metal oxide facets is highly sensitive to the specific spin arrangements. Even when all configurations are formally antiferromagnetic, variations in the noncollinear spin cancellation patterns can lead to substantial fluctuations in surface formation energy. [27,28] This sensitivity likely originates from interfacial effects involving subtle symmetry breaking, which can give rise to distinct surface spin textures. Within the field of antiferromagnetic spintronics, [29–31] such textures may arise from SOC mechanisms such as the spin Hall [32,33] and Rashba–Edelstein effects, [34] which provide a plausible explanation for the diverse spin configurations observed in our surface models.

This phenomenon introduces considerable complexity to subsequent calculations. To address this, we sampled several initial magnetic configurations on the FeO (100) facet. For the 2×2×5 supercell, the two magnetic configurations with in-plane cancellation along the *x*–*y* plane (stripy and canted Néel) exhibit similar surface energies per unit area (see **Table S4, Figure S14**). These configurations appear to be less favorable when the spin cancellation occurs along the *z* direction (perpendicular to the *x*–*y* plane), while the preference becomes slightly less pronounced in the larger simulation cell. Notably, the canted Néel configuration is hard to reproduce under periodic boundary conditions when transitioning to the 3×3×5 supercell and was thus excluded. Therefore,

the stripy configuration was selected as the reference for the clean surface energy in the subsequent adsorption calculations.

Table S4. Energetic comparison of non-collinear spin orderings on FeO(100).

Magnetic ensemble	Supercell	E_s (eV)	A (Å²)	E_s/A (eV/Å²)
stripy (*x*-*y* plane)	2×2×5	-4.307	38.369	-0.112
canted Néel (*x*-*y* plane)	2×2×5	-4.256	38.369	-0.111
z-axis	2×2×5	-3.235	38.369	-0.084
stripy (*x*-*y* plane)	3×3×5	-9.391	86.330	-0.109
z-axis	3×3×5	-9.321	86.330	-0.108

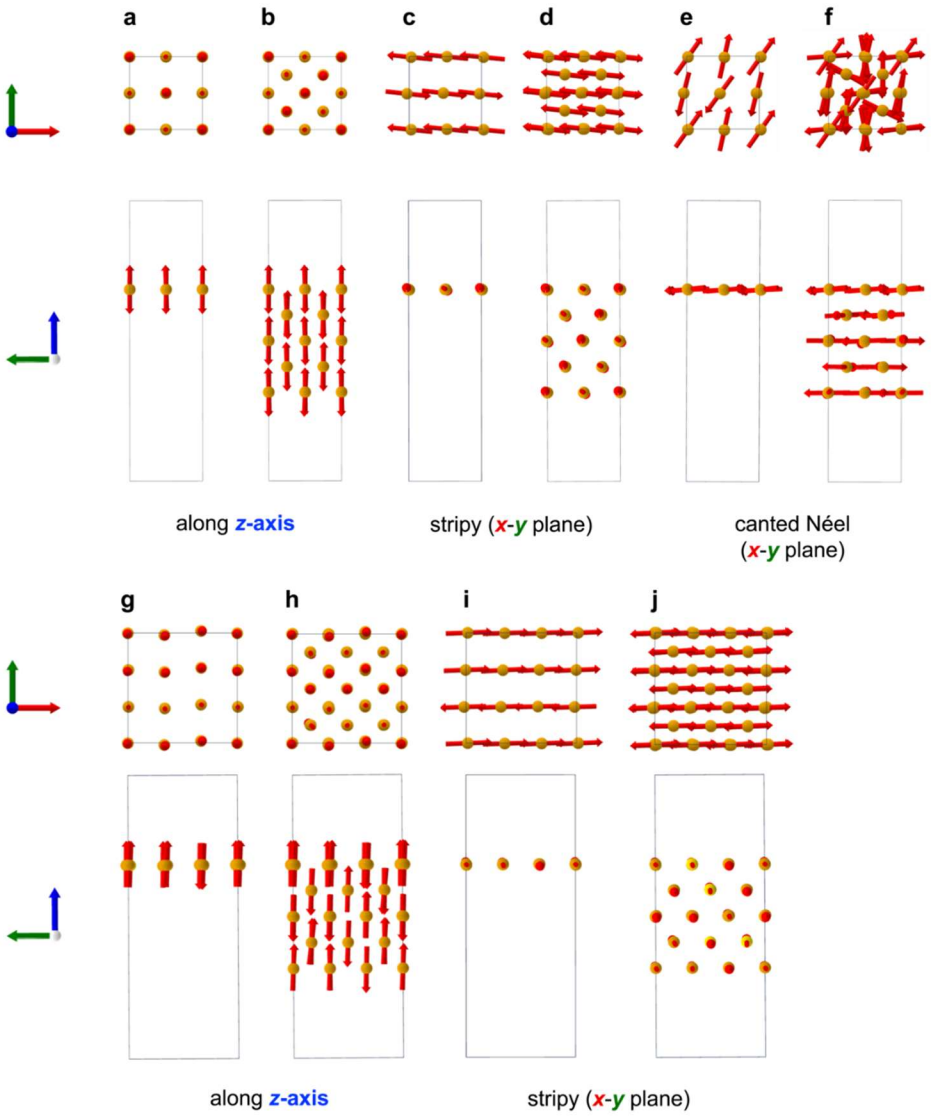

Figure S14. AFM configurations on relaxed FeO(100) clean surfaces: top and side views. Representative unit cells are outlined in gray; surface Fe atoms are shown as yellow spheres, and red arrows indicate non-collinear magnetic moments. Surface O atoms are omitted for clarity. Subplots a–f depicted three distinct spin patterns on 2×2 slabs, while g–j corresponded to those on 3×3 slabs. To highlight the AFM configurations nearest to active adsorption sites, subplots a, c, e, g, and i displayed only top-layer Fe MAGMOM vectors under different spin orders, whereas b, d, f, h, and j show the full-layer Fe MAGMOM vectors. Lattice axes shown as red (*a*), green (*b*), and blue (*c*) arrows.

Table S5. Monkhorst–Pack k-point meshes and corresponding computational objectives for material systems of varying sizes. *n* denotes the total number of atoms in the systems. *a* refers to the lattice constant (Å); E_{gap} indicates the band gap (eV); E_s denotes the cleaved surface formation energy (eV); μ_{Fe} represents the magnetic moment (μ_B) including non-collinear MAGMOM matrices for iron oxide systems; q_B indicates the Bader charge (e).

System	Size of cell/slab	*n*	*k*-point mesh	Target property
Fe (bulk)	primitive (cubic)	2	18×18×18	a
FeO (bulk)	primitive (cubic)	8	12×12×12	a, E_{gap}, μ_{Fe}, q_B
Fe_3O_4 (bulk)	primitive (rhombohedral)	14	10×10×10	μ_{Fe}, q_B
Fe(100)	2×2×5	20	9×9×1	E_s
Fe(110)	2×2×5	20	9×9×1	E_s
Fe(111)	2×2×5	20	7×7×1	E_s
FeO(100)	1×1×6	24	12×12×1	E_s, μ_{Fe}
FeO(110)	1×1×6	24	12×12×1	E_s, μ_{Fe}
FeO(111)	1×1×6	24	9×9×1	E_s, μ_{Fe}
Fe(100)	4×4×5	80	5×5×1	E_{ads}
FeO(100)	2×2×5	40	6×6×1	E_{ads}, μ_{Fe}
FeO(100)	3×3×5	90	3×3×1	E_{ads}, μ_{Fe}

Supplementary Note 5: Investigate the surface adsorption of the gaseous species

Next, we explore the surface reaction relevant to CO_2 reduction using DFT computations. In this stage, the D3BJ dispersion correction was explicitly included for both Fe(100) and FeO(100) surfaces to accurately account for van der Waals interactions between the adsorbates and the surfaces, which are otherwise underestimated in standard DFT treatments. [35,36] Various adsorption configurations and site characteristics of Fe(100) were listed in **Figures S15** and **Table S6**, including unit cell surface area (A), adsorption energies (E_{ads}), and site-specific geometric features. The adsorption energy (E_{ads}), was estimated using **Eq. S2**:

$$E_{ads} = E_{b*} - (E_{*} + E_{b}) \quad \textbf{Eq. S2}$$

where E_{b*} denotes the total energy of the relaxed surface–adsorbate complex, E_{*} represents the clean surface (with the surface state indicated by the subscript asterisk "*"), and E_{b} refers to the isolated adsorbate species (with the subscript "b" indicating the adsorbate). A negative value of E_{ads} signifies an exothermic adsorption process. In a similar manner, the dissociative adsorption energy of CO* and O* is denoted as ΔE_{chem}. [24]

$$\Delta E_{chem} = E_{CO^* + O^*} - (E_{*} + E_{CO_{2(g)}}) \quad \textbf{Eq. S3}$$

As an example, the most exothermic configuration on Fe (100) corresponds to adsorption at the H^4 site (where H denotes a 4-fold hollow site formed by surface Fe atoms, and the superscript ^{4} indicates four O–Fe coordination), yielding an E_{ads} of –0.92 eV. In contrast, the most endothermic adsorption occurs at the B^0 site, with an E_{ads} of +0.24 eV. Noted that Y. P. Ma and G. C. Wang, employing the BEEF exchange–correlation functional, [37] identified the same hollow adsorption configuration (corresponding to the H^4 site in **Table S6**) with a calculated E_{ads} of –0.69 eV. [38] Additionally, N. N. Tolkachev *et al*. reported a similar result at an nearly equivalent site using conventional PBE, which gave –0.87 eV. [39]

Table S6. Adsorption energetics and geometries on Fe(100). For the following tables, H, B and T denote 4-fold hollow, bridge and on-top sites, respectively. The $d_{A–B}$ (or $\bar{d}_{A–B}$) represents the (average) distance between atoms A and B. For CO_2*, $\bar{d}_{C–Fe}$ refers to the mean distance between the carbon atom and its bonded surface Fe atoms; $\bar{d}_{C–O}$ indicates the average internal C–O bond length within the CO_2 molecule; $\bar{d}_{O–Fe}$ describes the average distance between the oxygen atoms of CO_2 and the surface Fe atoms.

Surface	Supercell	A (Å²)	State	Site	E_{ads} (eV)	$\bar{d}_{C–Fe}$ (Å)	$\bar{d}_{C–O}$ (Å)	$\bar{d}_{O–Fe}$ (Å)	$\theta_{O–C–O}$ (°)
Fe(100)	4×4×5	131.152	CO_2*	T^2	-0.293	1.883	1.279	2.351	131.322
				B^2	-0.730	2.091	1.258	2.122	134.885
				B^0	0.242	2.090	1.268	-	132.268
				H^4	-0.923	2.175	1.343	2.073	120.925
				H^2	-0.562	2.193	1.318	1.957	118.171
						$\bar{d}_{C–Fe}$ (Å)	$d_{C–O}$ (Å)	$\bar{d}_{O–Fe}$ (Å)	
			CO*	T^0	-1.969	1.752	1.183	-	
				H^0	-1.092	2.183	1.235	-	
				H^2	-2.070	2.069	1.316	2.124	
						$\bar{d}_{O–Fe}$ (Å)			
			O*	T	-2.104	1.644			
				B	-2.723	1.821			
				H	-2.864	2.056			
					ΔE_{chem} (eV)				
			CO* + O*	T^0 + T	-0.788				
				T^0 + H	-1.720				
				H^2 + H	-1.769				

For FeO(100), following the analysis of magnetic ensembles on clean surfaces in the previous section, we extended similar considerations to examine the influence of post-adsorption magnetic

arrangements on adsorption energetics (the relaxed adsorption configurations are also provided in **Figure S16** and **S17)**. Interestingly, adsorption significantly alters the surface spin configurations and consistently favors AFM cancellation within the *x*–*y* plane rather than along the *z*-axis in almost all cases. We characterized the magnetic orders by projecting the MAGMOM vectors of top-layer Fe atoms onto the *x*–*y* plane, centered around the adsorbate. As summarized in **Table S7** (exemplified by a 2×2×5 supercell model), the observed patterns include stripy (antiparallel), zigzag, [40–42] vortex, [43–47] Néel, [48–58] and several biaxial variants of Néel and stripy ordering: canted Néel , [59–63] stripy Néel , crossed Néel and zigzag stripy. Noted that AFM configurations not strictly confined to the *x*–*y* plane, as well as those lacking discernible ordering, are categorized as "disordered," and only the most stable configuration from each category is presented.

The top views of representative unit cells with pattern-resolved magnetic moments were presented in **Figure S18** and **S19**. Though adsorbate-induced changes in surface spin arrangements may appear elusive, it is by no means unprecedented. Prior studies on simple hydrogen adsorption over transition metal surfaces have demonstrated that adsorption can significantly alter the overall magnetic strength of the material. [64–67] As shown in **Table S7**, we observed that even for similar adsorbate geometries and adsorption sites, variations in magnetic configurations can result in substantial fluctuations in calculated E_{ads}. Interestingly, among the most exothermic configurations, the FeO (100) surface itself tends to retain the stripy AFM patterns.

Table S7. Adsorption Energetics, magnetic properties and geometries on FeO(100). The notations follow those used in the last table. The label "phys" denoting configurations corresponding to physisorption, and the AFM spin pattern refers only to the spin arrangement of top-layer Fe atoms. For CO_2*, $d_{C–X}$ indicates the closest distance between the carbon atom in CO_2 and a surface element X—even for physisorbed states where no direct bonding is present. As an example, T(phys) denotes a configuration where the carbon atom in CO_2 is closest to a surface Fe on-top site, with a C–Fe distance of 3.322 Å.

Surface	Supercell	A (Å²)	State	Site	AFM pattern on x-y plane	E_{ads} (eV)	$d_{C–X}$ (Å)	$\bar{d}_{C–O}$ (Å)	$\bar{d}_{O–Fe}$ (Å)	$\theta_{O–C–O}$ (°)
				H^2	stripy	-0.441	1.431 (O)	1.261	2.177	132.509
				H^2	vortex	-0.407	1.429 (O)	1.262	2.167	132.376
				H^2	canted Néel	0.968	1.428 (O)	1.262	2.154	132.251
			CO_2*	T(phys)	canted Néel	-0.206	3.322 (Fe)	1.177	-	179.802
				H(phys)	Néel	0.256	2.899 (O)	1.177	-	177.951
				H(phys)	canted Néel	-0.330	2.900 (O)	1.177	-	177.681
				H(phys)	crossed Néel	-0.082	2.916 (O)	1.177	-	178.034
							$d_{C–Fe}$ (Å)	$d_{C–O}$ (Å)		
FeO(100)	2×2×5	38.369		T^0	Néel	-0.540	2.084	1.148		
			CO*	T^0	stripy Néel	-0.557	2.095	1.149		
				T^0	disordered	0.719	2.088	1.147		
							$\bar{d}_{O–Fe}$ (Å)			
				B	zigzag	-1.053	1.814			
			O*	B	Néel	-0.602	1.852			
				H(3-fold)	disordered	-0.775	1.986			
						ΔE_{chem} (eV)				
			CO* + O*	T^0 + B	zigzag stripy	1.568				

Surface	Supercell	A (Å²)	State	Site	AFM pattern on x-y plane	E_{ads} (eV)	$d_{C–X}$ (Å)	$\bar{d}_{C–O}$ (Å)	$\bar{d}_{O–Fe}$ (Å)	$\theta_{O–C–O}$ (°)
							$d_{C–X}$ (Å)	**$\bar{d}_{C–O}$ (Å)**	**$\bar{d}_{O–Fe}$ (Å)**	**$\theta_{O–C–O}$ (°)**
			CO_2*	H^2	canted stripy	-0.644	1.417 (O)	1.265	2.182	131.475
				H(phys)	stripy	-0.299	2.776 (O)	1.178	-	176.598
							$d_{C–Fe}$ (Å)	**$d_{C–O}$ (Å)**		
FeO(100)	3×3×5	86.330	CO*	T^0	disordered	0.523	2.083	1.149		
							$d_{O–Fe}$ (Å)			
			O*	T	stripy	0.043	1.678			
						ΔE_{chem} (eV)				
			CO* + O*	T^0 + T	stripy	2.512				

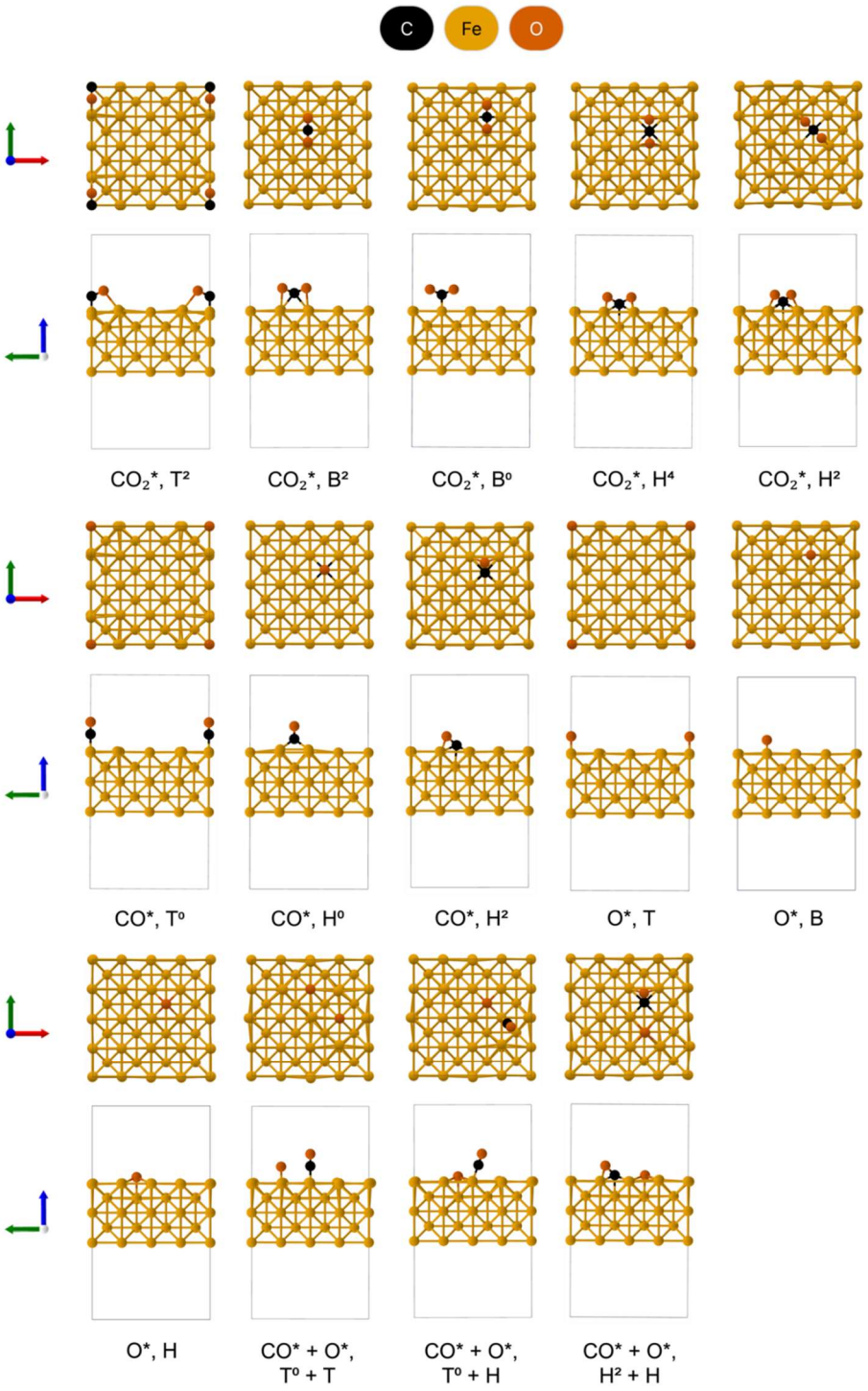

Figure S15. Top and side views of relaxed CO_2*, CO*, O*, and CO* + O* adsorption configurations on the 4×4×5 Fe(100) surface. Lattice axes shown as red (*a*), green (*b*), and blue (*c*) arrows.

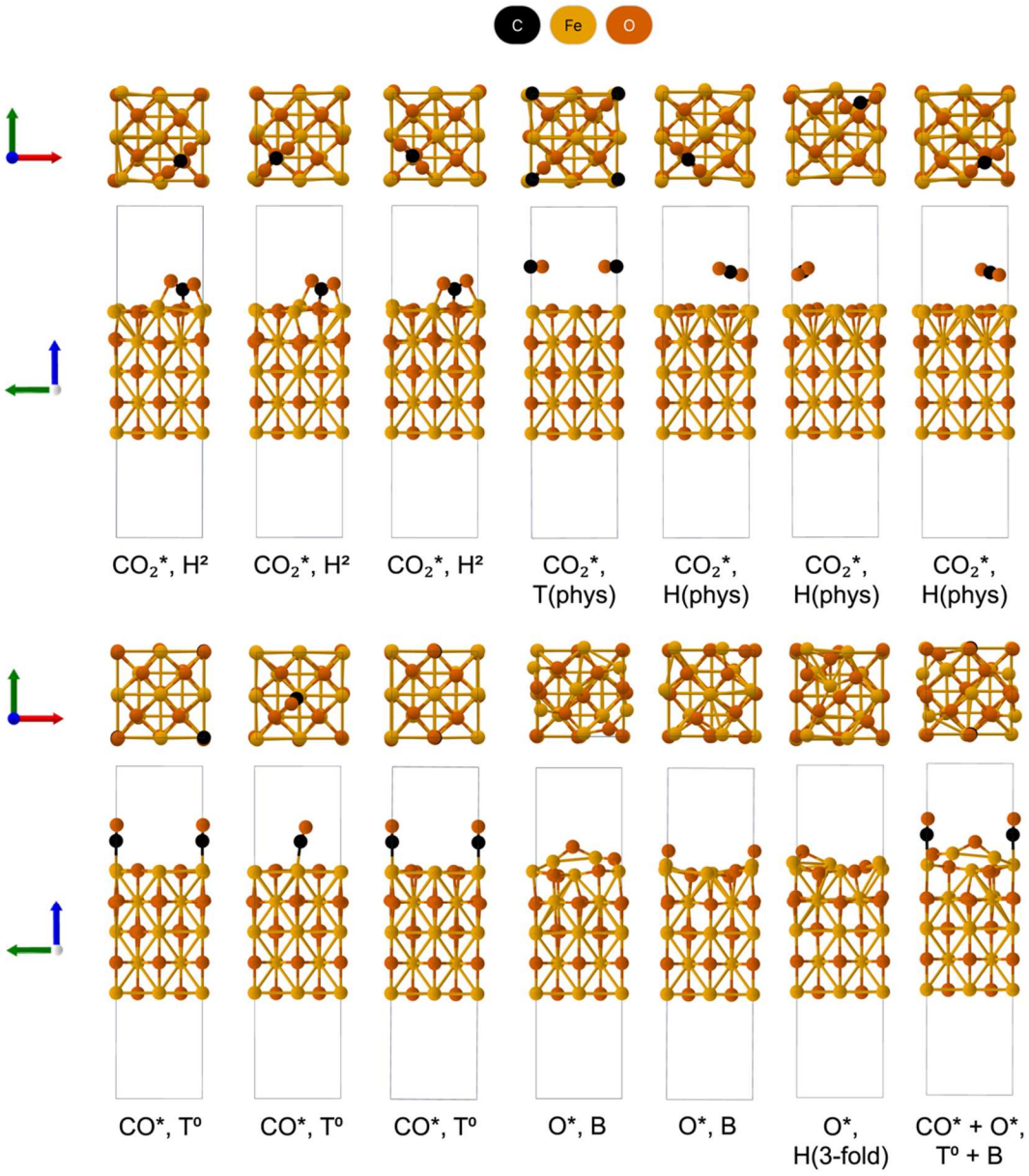

Figure S16. Top and side views of relaxed CO_2*, CO*, O*, and CO* + O* adsorption configurations on the 2×2×5 FeO(100) surface. Lattice axes shown as red (*a*), green (*b*), and blue (*c*) arrows.

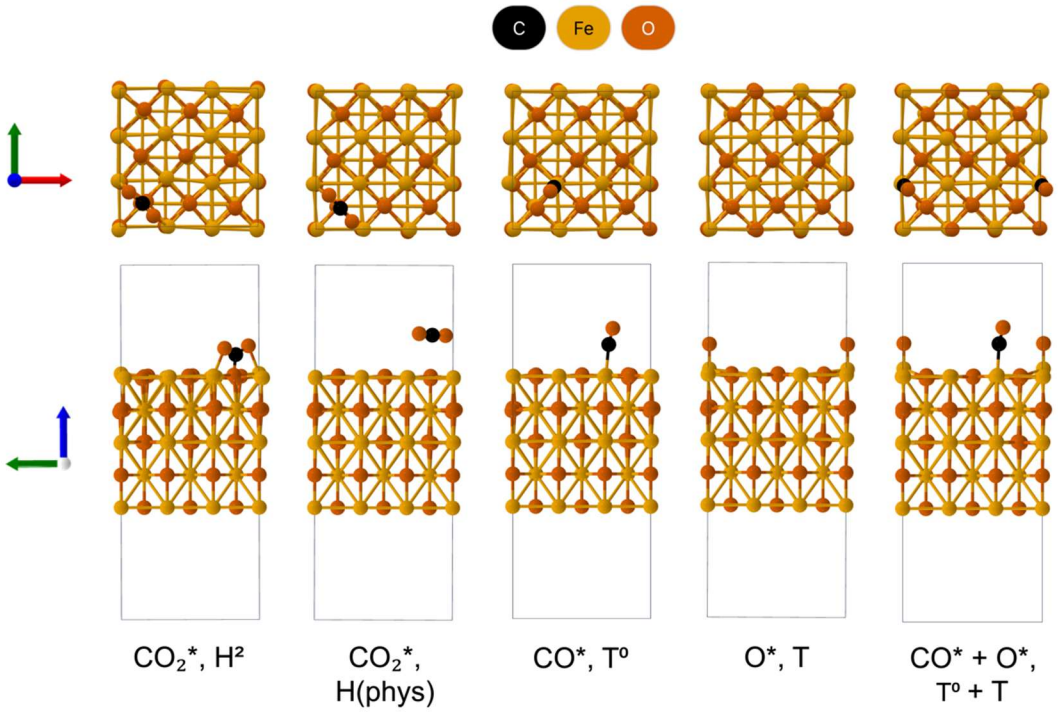

Figure S17. Top and side views of relaxed CO_2*, CO*, O*, and CO* + O* adsorption configurations on the 3×3×5 FeO(100) surface. Lattice axes shown as red (*a*), green (*b*), and blue (*c*) arrows.

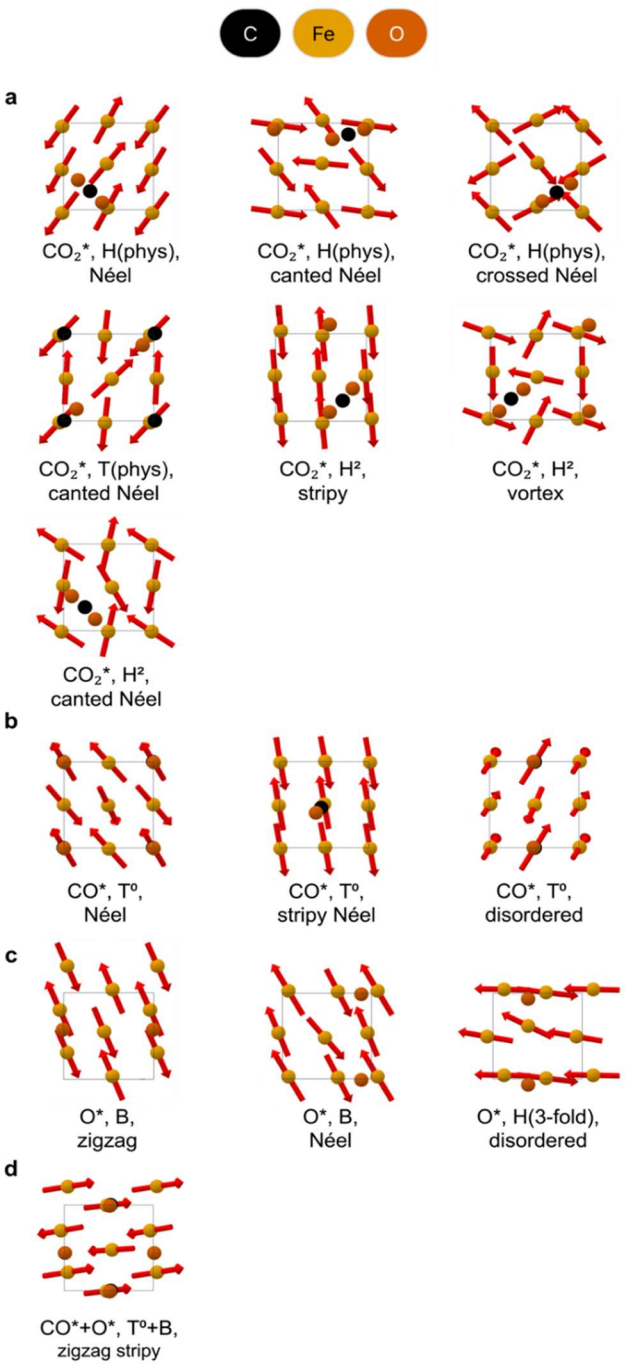

Figure S18. Top-layer AFM configurations on 2×2 FeO(100). Representative unit cells (gray lines) show magnetic moments (red arrows) for top-layer Fe atoms (yellow; O atoms omitted for clarity) and adsorbates (C: black; O: orange). Panels a–d correspond to CO_2*, CO*, O*, and dissociated CO* + O* states, respectively.

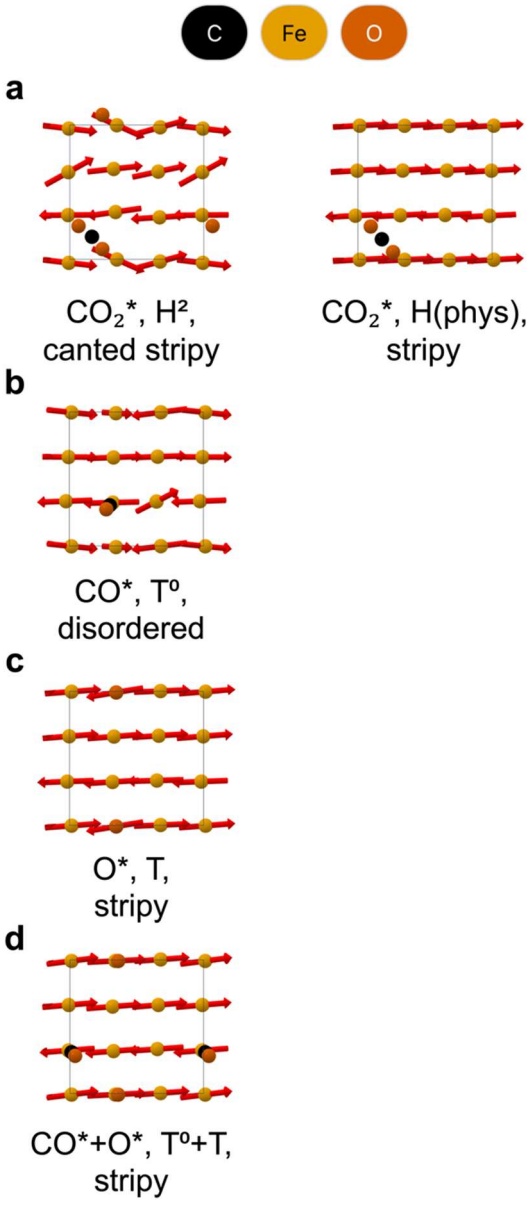

Figure S19. Top-layer AFM configurations on 3×3 FeO(100). Representative unit cells (gray lines) show magnetic moments (red arrows) for top-layer Fe atoms (yellow; O atoms omitted for clarity) and adsorbates (C: black; O: orange). Panels a–d correspond to CO_2*, CO*, O*, and dissociated CO* + O* states, respectively.

Supplementary Note 6: The reaction energy diagram

As discussed in previous sections, CO_2 reduction reaction (CO_2RR) on both materials involves CO_2 adsorption (CO_2*), dissociative adsorption of CO_2 where the C–O bond breaks to form co-adsorbed CO* and O*, as well as individual adsorption of CO* or O*. Accordingly, **Figure 5** summarizes the reaction energy diagrams associated with these intermediates on various surfaces, while **Figure 5c** specifically only reflects the results obtained using a 2×2×5 FeO(100) supercell. As a supplement, **Figure S20** shows the reaction pathway on a 3×3×5 FeO(100) surface, emphasizing the influence of lower adsorbate coverage on reaction energetics (1/9 ML in **Figure S21** vs. 1/4 ML in **Figure 5c**).

At a coverage of 1/9 ML, the C–O bond cleavage following the CO_2 chemisorption appears more difficult, with an energy difference of +3.16 eV compared to +2.01 eV at 1/4 ML. This can be attributed to the reduced stabilization of the resulting O* and CO* intermediates at lower coverage, as reflected by their nearly thermoneutral or exergonic desorption energies (O* = –0.04 eV, CO* = –0.52 eV), in contrast to the more stabilized state at 1/4 ML (O* = +1.05 eV, CO* = +0.56 eV).

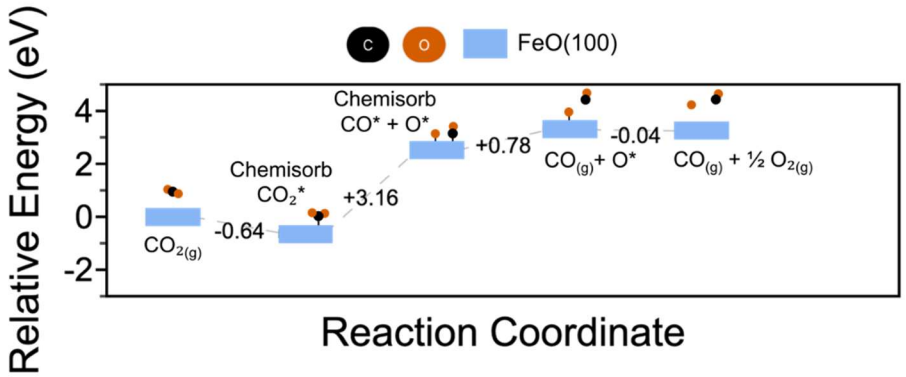

Figure S20. Reaction energy diagrams for CO_2 reduction on 3×3×5 FeO(100) slab model.

Supplementary Note 7: The CO* spillover at Fe/FeO interface and the effect of coverage

As shown in **Figure 5c** and **S20**, the dissociation of CO_2 on FeO(100) is highly endergonic regardless of slab size, indicating its much lower efficiency in breaking C–O bond as compared to Fe(100). To address this, we considered the possibility of surface CO* spillover between coexisting Fe and FeO surfaces, as discussed in the main text. This process involves CO_2 dissociation occurring on Fe (100), followed by spillover of the resulting CO* species onto the FeO (100) surface. The energies in **Figure 5a** were derived from surface energy calculations using a combined Fe(100)/2×2 FeO(100) system. The energy difference of the CO^* spillover is estimated using **Eq. S4**:

$$\Delta E_{\text{spillover}} = (E_{\text{CO*, FeO(100)}} + E_{*,\text{ Fe(100)}}) - (E_{\text{CO*, Fe(100)}} + E_{*,\text{ FeO(100)}}) \qquad \textbf{Eq. S4}$$

where $\Delta E_{\text{spillover}}$ indicates the tendency of CO* species to migrate from one surface to another, $E_{\text{CO*}}$ denotes the adsorption energy of CO and E_* refers to the total energy of the clean surface. In contrast, for the combined Fe(100)/3×3 FeO(100) system, we encountered difficulty in reaching a converged result. Accordingly, the exchange process was approximated by **Eq. S5**:

$$\Delta E_{\text{spillover}} = (E_{\text{CO*+O*, FeO(100)}} + E_{\text{O*, Fe(100)}}) - (E_{\text{CO*+O*, Fe(100)}} + E_{\text{O*, FeO(100)}}) \qquad \textbf{Eq. S5}$$

which captures the thermodynamic driving force for CO transfer from Fe(100) to the bare FeO(100) surface in the presence of a dangling O* intermediate on the interface. $E_{\text{CO*+O*}}$ and $E_{\text{O*}}$ denote the energies of co-adsorbed CO* + O* and individual O*, respectively.

To investigate whether CO adsorption on Fe(100) remains strongly favorable (a key factor for supporting the suggested spillover effect), we further evaluated the thermodynamic preference for desorbing a single CO molecule from Fe(100) at different coverages. The adsorption energies shown in **Figure S21** were obtained from the configurations listed in **Figure S22**, where all adsorption sites were initialized from the most stable state (e.g., H^2) identified in **Table S6**. For CO coverages ($\theta_{\text{CO*}}$) of 1/4, 1/2, 3/4, and 1 monolayer (ML), each arrangement was designed to

maximize intermolecular spacing, leading to symmetric adsorption patterns and only one configuration being relaxed per coverage in our calculations. As coverage exceeds 1/2 ML, CO–CO interactions become significant, preventing the adsorbates from lying flat. At 1 ML, all CO* species adopt upright geometries to better minimize repulsion.

The coverage test reveals that at approximately 3/4 ML, CO adsorption becomes slightly less exothermic (dropping from a maximum of –2.15 eV to –1.72 eV) yet still satisfies the thermodynamic condition for enabling the spillover effect (i.e., adsorption remains stronger than –1.59 eV). Additionally, we compared these results with prior PBE calculations without D3(BJ) dispersion corrections reported by T. Wang *et al*., [25] as shown in **Figure S20**. While adsorption energies at low θ_{CO*} are nearly identical, our calculated E_{ads} at higher θ_{CO*} is more negative (likely due to van der Waals contributions). Nevertheless, both approaches exhibit similar trends and adsorption geometries across θ_{CO*}, reinforcing the robustness of this conclusion. Moreover, they also revealed that even on Fe (110) and Fe (111), high θ_{CO*} lead to desorption and C–O bond dissociation barriers that exceed the threshold required for spillover (~1.6 eV). For instance, at 5/12 ML coverage on Fe(110), a single CO desorption exhibits a barrier of 1.56 eV, while C–O bond cleavage to form C* and O* incurs a barrier of 1.70 eV. [26]

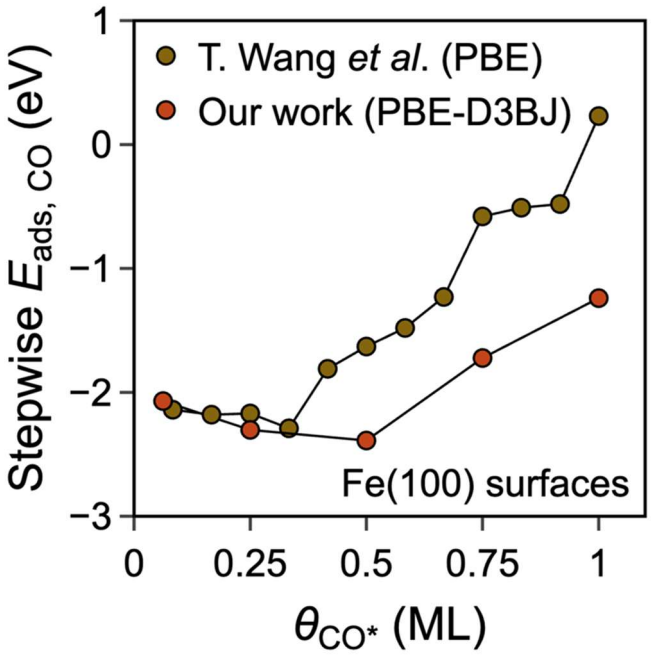

Figure S21. Comparison of stepwise CO adsorption energy at different coverages on Fe (100) surfaces.

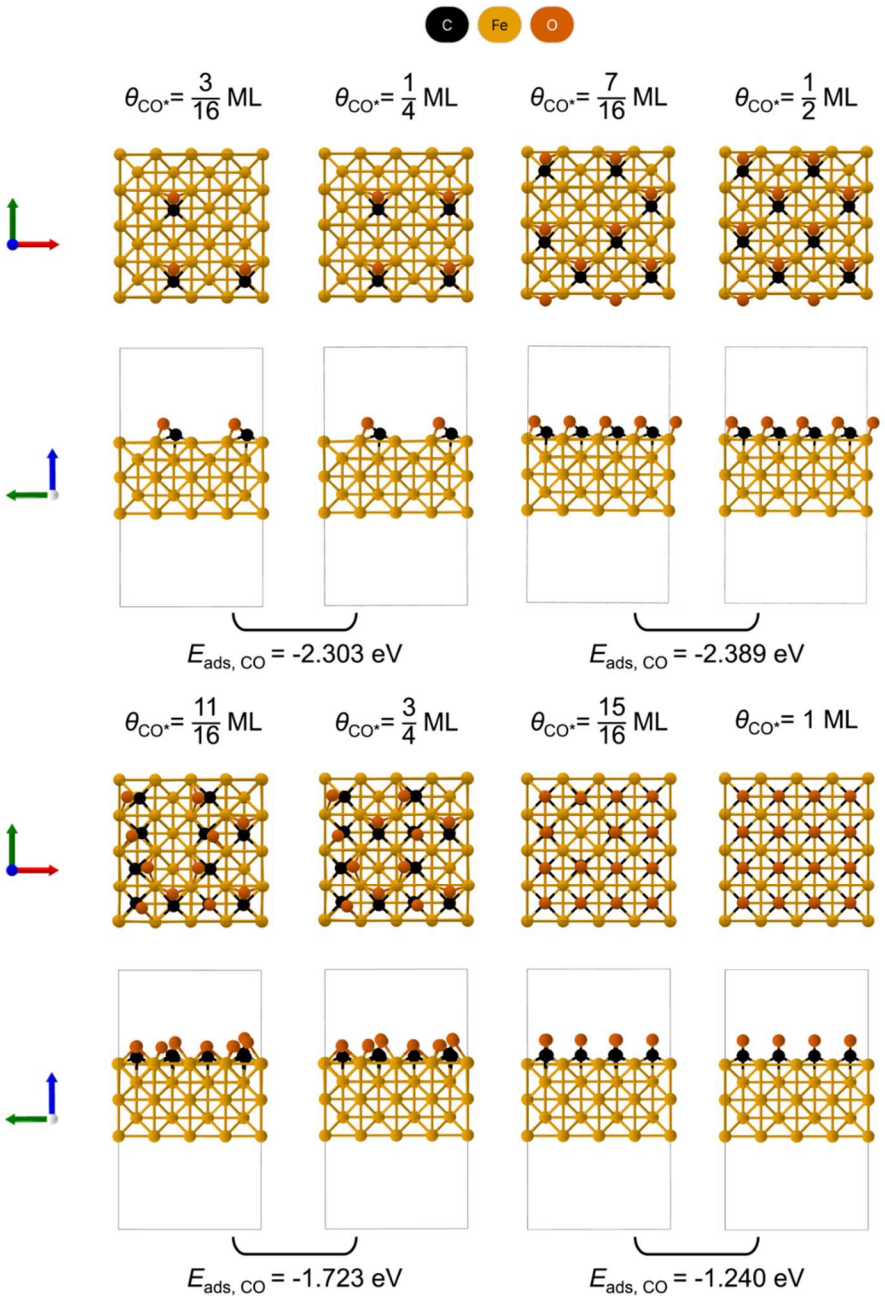

Figure S22. Stepwise adsorption configurations and energetics of CO on Fe(100) under varying coverages. Top and side views of relaxed CO adsorption structures on a 4×4×5 Fe(100) slab at different θ_{CO^*} (ML) are shown. The corresponding stepwise adsorption free energies ($E_{ads, CO}$) are reported for transitions from 3/16 to 1/4, 7/16 to 1/2, 11/16 to 3/4, and 15/16 to 1 ML coverage. Lattice axes shown as red (*a*), green (*b*), and blue (*c*) arrows.

Supplementary Note 8: Surface reconstruction on FeO (100)

We observed a notable phenomenon during the relaxation of the 2×2 FeO(100) slab: adsorption of O* induces significant surface reconstruction (**Figure S23**). The top-layer Fe atoms tend to adopt a coordination environment resembling that in Fe_3O_4, characterized by a lower average Fe–O* coordination number. As shown in **Table S7**, the most exothermic O* bridge adsorption state (E_{ads} = –1.053 eV) corresponds to exactly 4-fold coordination, while moderately exothermic (–0.775 eV) and endothermic (–0.602 eV) states exhibit coordination numbers of 4.25 and 4.5, respectively. To further understand this behavior, we compared the Bader charges of surface Fe atoms in the O*-adsorbed 2×2 FeO(100) with those in clean FeO surfaces and bulk Fe_3O_4 (**Figure S15c**). The average net charge of Fe (q_{Fe}) increases from the uniform ~1.3 e in bulk and clean FeO to a broader distribution (q_{Fe} = 1.223–1.600 e) upon O* adsorption. This bader charge resembles that in bulk Fe_3O_4, where two Fe atoms exhibit Fe^{2+}-like states ($q_{Fe} \approx +1.362$ e) and four show Fe^{3+}-like states ($q_{Fe} \approx +1.649$ e), suggesting a tendency of the FeO(100) surface to evolve toward a higher oxidation state akin to Fe_3O_4 in the final stages of the CO_2 reduction pathway.

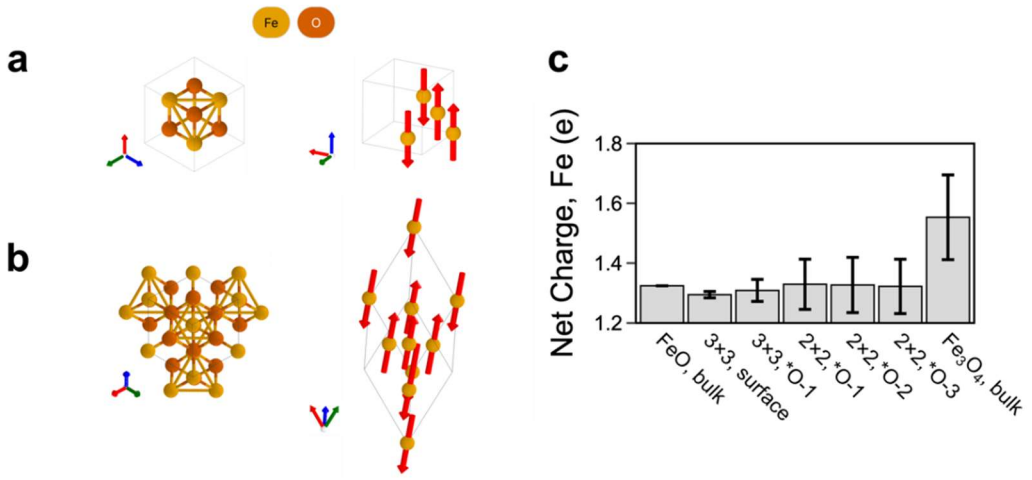

Figure S23. Computational setup and Bader charge analysis related to surface reconstruction. a,b) Relaxed bulk structures of FeO and Fe_3O_4 with corresponding non-collinear spin configurations (O atoms omitted for clarity). Gray lines denote the unit cell boundaries. The Fe_3O_4 setup follows the final selection listed in Table S1. c) Average net Bader charges of Fe atoms (q_{Fe}, in e) across systems are shown as bars, with standard deviations indicated by error bars. Lattice axes shown as red (*a*), green (*b*), and blue (*c*) arrows.

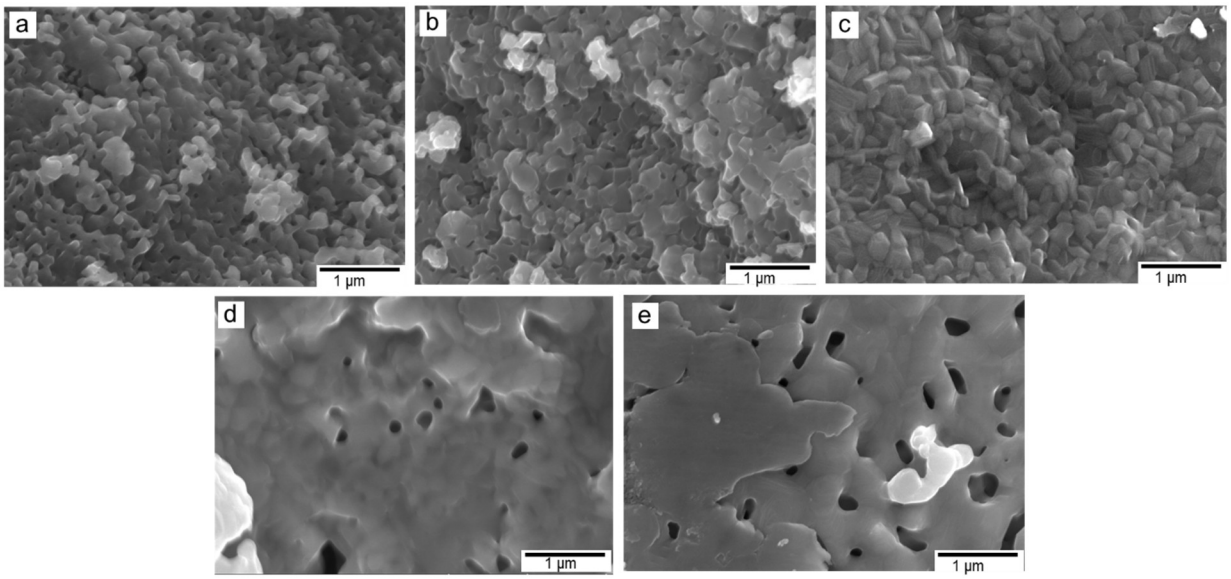

Figure S24. Representative SEM micrographs of the used oxygen carrier after the 8th H_2 step.

(a) 3 min / 10 min, (b) 5min / 10 min, (c) 7 min / 10 min, and (d) 10 min / 10 min program. (e) After the 3rd H_2 step of the 60 min / 10 min program.

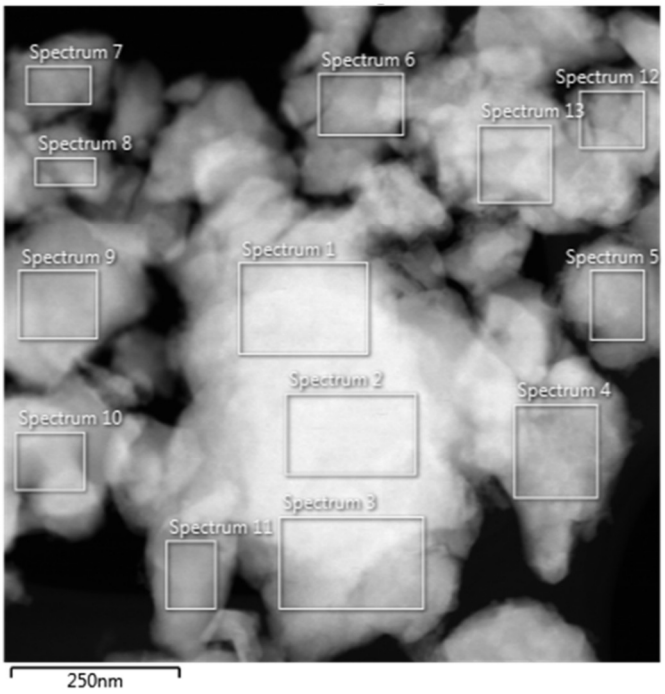

Spectrum	Fe-Atomic%	O-Atomic%
1	39	61
2	39.2	60.8
3	35.5	64.5
4	39.8	60.2
5	42.6	57.4
6	39.5	60.5
7	37.2	62.8
8	38.3	61.7
9	41.6	58.4
10	39.1	60.9
11	32.9	67.1
12	43.7	56.3
13	39.2	60.8

Figure S25. STEM and EDS spot analysis of the crushed oxygen carrier after the 8th H_2 step of the 3 min / 10 min program.

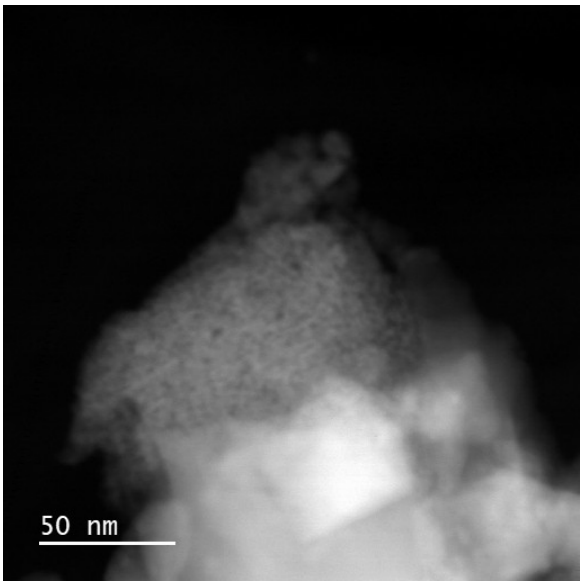

Figure S26. HAADF-STEM image of the crushed oxygen carrier taken after the reduction step of the 8th cycle of the 3 min / 10 min program.

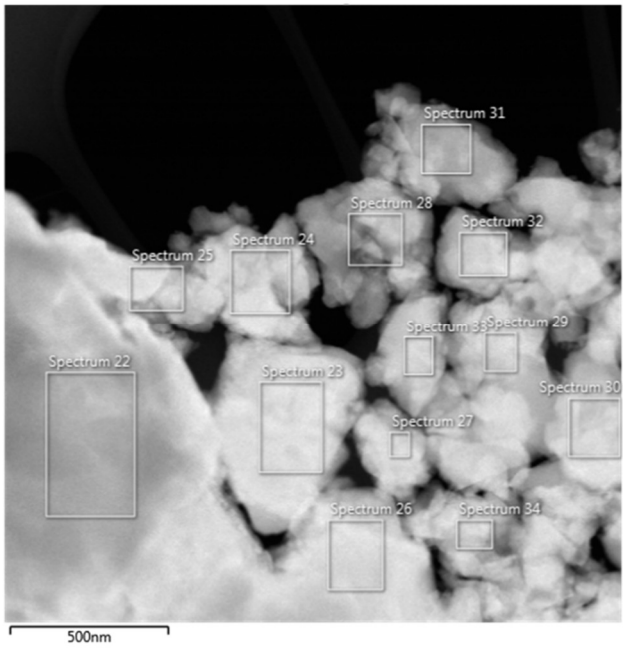

Spectrum	Fe-Atomic%	O-Atomic%
22	73.9	26.1
23	48.6	51.4
24	38.3	61.7
25	51.8	48.2
26	56.3	43.7
27	44.3	55.7
28	38.7	61.3
29	42.5	57.5
30	50.1	49.9
31	37.1	62.9
32	40.2	59.8
33	43.9	56.1
34	42.8	57.2

Figure S27. STEM and EDS spot analysis of the crushed oxygen carrier after the 8th H_2 step of the 5 min / 10 min program.

References

1. Liao, P. & Carter, E. A. Ab initio DFT + U predictions of tensile properties of iron oxides. *J. Mater. Chem.* **20**, 6703 (2010).
2. Zhou, F., Cococcioni, M., Marianetti, C. A., Morgan, D. & Ceder, G. First-principles prediction of redox potentials in transition-metal compounds withLDA+U. *Phys. Rev. B* **70**, (2004).
3. Cococcioni, M. & De Gironcoli, S. Linear response approach to the calculation of the effective interaction parameters in theLDA+Umethod. *Phys. Rev. B* **71**, (2005).
4. Wang, L., Maxisch, T. & Ceder, G. Oxidation energies of transition metal oxides within theGGA+Uframework. *Phys. Rev. B* **73**, (2006).
5. Mosey, N. J., Liao, P. & Carter, E. A. Rotationally invariant *ab initio* evaluation of Coulomb and exchange parameters for DFT+U calculations. *J. Chem. Phys.* **129**, (2008).
6. Xia, W. *et al.* Machine Learning Model for the Prediction of Hubbard *U* Parameters and Its Application to Fe–O Systems. *J. Chem. Theory Comput.* **20**, 10095–10102 (2024).
7. None Available. Materials Data on FeO by Materials Project. LBNL Materials Project; Lawrence Berkeley National Laboratory (LBNL), Berkeley, CA (United States) https://doi.org/10.17188/1193609 (2020).
8. Tombs, N. C. & Rooksby, H. P. Structure of Monoxides of some Transition Elements at Low Temperatures. *Nature* **165**, 442–443 (1950).
9. Roth, W. L. Magnetic Structures of MnO, FeO, CoO, and NiO. *Phys. Rev.* **110**, 1333–1341 (1958).
10. Battle, P. D. & Cheetham, A. K. The magnetic structure of non-stoichiometric ferrous oxide. *J. Phys. C Solid State Phys.* **12**, 337–345 (1979).

11. McCammon, C. A. & Liu, L. The effects of pressure and temperature on nonstoichiometric wustite, Fe_xO: The iron-rich phase boundary. *Phys. Chem. Miner.* **10**, 106–113 (1984).
12. Alfredsson, M. *et al.* Electronic structure of the antiferromagneticB1-structured FeO. *Phys. Rev. B* **70**, (2004).
13. Tran, F., Blaha, P., Schwarz, K. & Novák, P. Hybrid exchange-correlation energy functionals for strongly correlated electrons: Applications to transition-metal monoxides. *Phys. Rev. B* **74**, (2006).
14. Zhang, W.-B., Deng, Y.-H., Hu, Y.-L., Han, K.-L. & Tang, B.-Y. Structural distortion of B1-structured MnO and FeO. *Solid State Commun.* **142**, 6–9 (2007).
15. Zhong, H. *et al.* The adsorption behaviors of CO and H2 on FeO surface: A density functional theory study. *Powder Technol.* **303**, 100–108 (2016).
16. Liang, Z. *et al.* Effect of Silica on Reduction Behaviors of Hematite-carbon Composite Compact at 1223–1373 K. *ISIJ Int.* **59**, 227–234 (2019).
17. Forti, M., Alonso, P., Gargano, P. & Rubiolo, G. Transition Metals Monoxides. An LDA+U Study. *Procedia Mater. Sci.* **1**, 230–234 (2012).
18. Bowen, H. K., Adler, D. & Auker, B. H. Electrical and optical properties of FeO. *J. Solid State Chem.* **12**, 355–359 (1975).
19. Balberg, I. & Pinch, H. L. The optical absorption of iron oxides. *J. Magn. Magn. Mater.* **7**, 12–15 (1978).
20. Wei, P. & Qi, Z. Q. Insulating gap in the transition-metal oxides: A calculation using the local-spin-density approximation with the on-site Coulomb*U*correlation correction. *Phys. Rev. B* **49**, 10864–10868 (1994).

21. Mazin, I. I. & Anisimov, V. I. Insulating gap in FeO: Correlations and covalency. *Phys. Rev. B* **55**, 12822–12825 (1997).
22. Gramsch, S. A., Cohen, R. E. & Savrasov, S. Y. Structure, metal-insulator transitions, and magnetic properties of FeO at high pressures. *Am. Mineral.* **88**, 257–261 (2003).
23. Eom, T., Lim, H.-K., Goddard, W. A. & Kim, H. First-Principles Study of Iron Oxide Polytypes: Comparison of GGA+*U* and Hybrid Functional Method. *J. Phys. Chem. C* **119**, 556–562 (2015).
24. Liu, X., Sun, L. & Deng, W.-Q. Theoretical Investigation of CO_2 Adsorption and Dissociation on Low Index Surfaces of Transition Metals. *J. Phys. Chem. C* **122**, 8306–8314 (2018).
25. Wang, T. *et al.* High Coverage CO Activation Mechanisms on Fe(100) from Computations. *J. Phys. Chem. C* **118**, 1095–1101 (2014).
26. Wang, T. *et al.* Coverage-Dependent CO Adsorption and Dissociation Mechanisms on Iron Surfaces from DFT Computations. *ACS Catal.* **4**, 1991–2005 (2014).
27. Yoon, S. *et al.* A “non-dynamical” way of describing room-temperature paramagnetic manganese oxide. *Phys. Chem. Chem. Phys.* **21**, 15932–15939 (2019).
28. Yoon, S. *et al.* Effects of paramagnetic fluctuations on the thermochemistry of MnO(100) surfaces in the oxygen evolution reaction. *Phys. Chem. Chem. Phys.* **23**, 859–865 (2021).
29. Jungwirth, T., Marti, X., Wadley, P. & Wunderlich, J. Antiferromagnetic spintronics. *Nat. Nanotechnol.* **11**, 231–241 (2016).
30. Baltz, V. *et al.* Antiferromagnetic spintronics. *Rev. Mod. Phys.* **90**, (2018).
31. Železný, J., Wadley, P., Olejník, K., Hoffmann, A. & Ohno, H. Spin transport and spin torque in antiferromagnetic devices. *Nat. Phys.* **14**, 220–228 (2018).

32. Dyakonov, M. I. & Perel, V. I. Current-induced spin orientation of electrons in semiconductors. *Phys. Lett. A* **35**, 459–460 (1971).
33. Hirsch, J. E. Spin Hall Effect. *Phys. Rev. Lett.* **83**, 1834–1837 (1999).
34. Edelstein, V. M. Spin polarization of conduction electrons induced by electric current in two-dimensional asymmetric electron systems. *Solid State Commun.* **73**, 233–235 (1990).
35. Grimme, S., Antony, J., Ehrlich, S. & Krieg, H. A consistent and accurate*ab initio*parametrization of density functional dispersion correction (DFT-D) for the 94 elements H-Pu. *J. Chem. Phys.* **132**, (2010).
36. Grimme, S., Ehrlich, S. & Goerigk, L. Effect of the damping function in dispersion corrected density functional theory. *J. Comput. Chem.* **32**, 1456–1465 (2011).
37. Wellendorff, J. *et al.* Density functionals for surface science: Exchange-correlation model development with Bayesian error estimation. *Phys. Rev. B* **85**, (2012).
38. Ma, Y.-P. & Wang, G.-C. Comparative theoretical study of CO2 activation on clean and potassium-preadsorbed low index surfaces of transition metals. *J. Mol. Model.* **29**, (2023).
39. Tolkachev, N. N., Pokusaeva, Ya. A. & Bogdan, V. I. DFT Study of Potential Barriers and Trajectory of CO2 Adsorption/Desorption As Well As Dissociation on Clusters Simulating Fe (100), Fe (110), and Fe (111) Facets. *Russ. J. Phys. Chem. A* **97**, 1782–1791 (2023).
40. Mazin, I. I., Jeschke, H. O., Foyevtsova, K., Valenti, R. & Khomskii, D. I. Na2IrO3 as a molecular orbital crystal. (2012) doi:10.48550/ARXIV.1205.0434.
41. Kim, H.-J., Lee, J.-H. & Cho, J.-H. Antiferromagnetic Slater Insulator Phase of Na2IrO3. *Sci. Rep.* **4**, (2014).
42. Yadav, P. *et al.* Role of local structural distortions on the origin of j=1/2 pseudo-spin state in sodium iridate. Preprint at https://doi.org/10.48550/ARXIV.2205.05902 (2022).

43. Mentink, S. A. M. *et al.* Magnetic Ordering and Frustration in Hexagonal UNi4B. *Phys. Rev. Lett.* **73**, 1031–1034 (1994).
44. Saito, H. *et al.* Evidence of a New Current-Induced Magnetoelectric Effect in a Toroidal Magnetic Ordered State of UNi_4B. *J. Phys. Soc. Jpn.* **87**, 033702 (2018).
45. Yanagisawa, T. *et al.* Electric Quadrupolar Contributions in the Magnetic Phases of UNi4B. *Phys. Rev. Lett.* **126**, (2021).
46. Ishitobi, T. & Hattori, K. Triple-Q partial magnetic orders induced by quadrupolar interactions: Triforce order scenario for UNi4B. *Phys. Rev. B* **107**, (2023).
47. Hayami, S. Spontaneous Magnetization Induced by Antiferromagnetic Toroidal Ordering. *Nanomaterials* **14**, 1729 (2024).
48. Wadley, P. *et al.* Electrical switching of an antiferromagnet. *Science* **351**, 587–590 (2016).
49. Bodnar, S. Yu. *et al.* Writing and reading antiferromagnetic Mn2Au by Néel spin-orbit torques and large anisotropic magnetoresistance. *Nat. Commun.* **9**, (2018).
50. Chen, X. Z. *et al.* Antidamping-Torque-Induced Switching in Biaxial Antiferromagnetic Insulators. *Phys. Rev. Lett.* **120**, (2018).
51. Meinert, M., Graulich, D. & Matalla-Wagner, T. Electrical Switching of Antiferromagnetic Mn2Au and the Role of Thermal Activation. *Phys. Rev. Appl.* **9**, (2018).
52. Moriyama, T., Oda, K., Ohkochi, T., Kimata, M. & Ono, T. Spin torque control of antiferromagnetic moments in NiO. *Sci. Rep.* **8**, (2018).
53. Gray, I. *et al.* Spin Seebeck Imaging of Spin-Torque Switching in Antiferromagnetic Pt/NiO Heterostructures. *Phys. Rev. X* **9**, (2019).
54. Baldrati, L. *et al.* Mechanism of Néel Order Switching in Antiferromagnetic Thin Films Revealed by Magnetotransport and Direct Imaging. *Phys. Rev. Lett.* **123**, (2019).

55. Schreiber, F. *et al.* Concurrent magneto-optical imaging and magneto-transport readout of electrical switching of insulating antiferromagnetic thin films. *Appl. Phys. Lett.* **117**, (2020).
56. Sass, P. M. *et al.* Magnetic Imaging of Domain Walls in the Antiferromagnetic Topological Insulator $MnBi_2Te_4$. *Nano Lett.* **20**, 2609–2614 (2020).
57. Meer, H. *et al.* Direct Imaging of Current-Induced Antiferromagnetic Switching Revealing a Pure Thermomagnetoelastic Switching Mechanism in NiO. *Nano Lett.* **21**, 114–119 (2021).
58. Takeuchi, Y. *et al.* Chiral-spin rotation of non-collinear antiferromagnet by spin–orbit torque. *Nat. Mater.* **20**, 1364–1370 (2021).
59. Jackeli, G. & Khaliullin, G. Mott Insulators in the Strong Spin-Orbit Coupling Limit: From Heisenberg to a Quantum Compass and Kitaev Models. *Phys. Rev. Lett.* **102**, (2009).
60. Fujiyama, S. *et al.* Two-Dimensional Heisenberg Behavior ofJeff=1/2Isospins in the Paramagnetic State of the Spin-Orbital Mott InsulatorSr2IrO4. *Phys. Rev. Lett.* **108**, (2012).
61. Liu, P. *et al.* Anisotropic magnetic couplings and structure-driven canted to collinear transitions inSr2IrO4by magnetically constrained noncollinear DFT. *Phys. Rev. B* **92**, (2015).
62. Owerre, S. A. Noncollinear antiferromagnetic Haldane magnon insulator. *J. Appl. Phys.* **121**, (2017).
63. Arakawa, N. Magnon drag induced by magnon-magnon interactions characteristic of noncollinear magnets. *Phys. Rev. B* **106**, (2022).
64. Greeley, J. & Mavrikakis, M. A first-principles study of surface and subsurface H on and in Ni(111): diffusional properties and coverage-dependent behavior. *Surf. Sci.* **540**, 215–229 (2003).
65. Bessarab, P. F., Uzdin, V. M. & Jónsson, H. Effect of hydrogen adsorption on the magnetic properties of a surface nanocluster of iron. *Phys. Rev. B* **88**, 214407 (2013).

66. López, M. J., Blanco-Rey, M., Juaristi, J. I., Alducin, M. & Alonso, J. A. Manipulating the Magnetic Moment of Palladium Clusters by Adsorption and Dissociation of Molecular Hydrogen. *J. Phys. Chem. C* **121**, 20756–20762 (2017).
67. Melander, M. & Jónsson, H. Effect of H adsorption on the magnetic properties of an Fe island on a W(110) surface. *Phys. Rev. B* **100**, 174431 (2019).